

Tantalizing Evidence of Reionization Relics in the eBOSS DR16 Ly α Forest Correlations: a Preference for Early Reionization

Yifan Zheng,¹ Paulo Montero-Camacho,^{2*} Zheng Cai^{1,2} and Yi Mao^{1†}

¹*Department of Astronomy, Tsinghua University, Beijing 100084, China*

²*Department of Mathematics and Theory, Peng Cheng Laboratory, Shenzhen, Guangdong 518066, China*

Accepted XXX. Received YYY; in original form ZZZ

ABSTRACT

Cosmic reionization of H I leaves enduring relics in the post-reionization intergalactic medium, potentially influencing the Lyman- α (Ly α) forest down to redshifts as low as $z \approx 2$, which is the so-called “memory of reionization” effect. Here, we re-analyze the baryonic acoustic oscillation (BAO) measurements from Ly α absorption and quasar correlations using data from the extended Baryonic Oscillation Spectroscopic Survey (eBOSS) Data Release 16 (DR16), incorporating for the first time the memory of reionization in the Ly α forest. Three distinct scenarios of reionization timeline are considered in our analyses. We find that the recovered BAO parameters (α_{\parallel} , α_{\perp}) remain consistent with the original eBOSS DR16 analysis. However, models incorporating reionization relics provide a better fit to the data, with a tantalizing preference for early reionization, consistent with recent findings from the James Webb Space Telescope. Furthermore, the inclusion of reionization relics significantly impacts the non-BAO parameters. For instance, we report deviations of up to 3σ in the Ly α redshift-space distortion parameter and $\sim 7\sigma$ in the linear Ly α bias for the late reionization scenario. Our findings suggest that the eBOSS Ly α data is more accurately described by models that incorporate a broadband enhancement to the Ly α forest power spectrum, highlighting the importance of accounting for reionization relics in cosmological analyses.

Key words: dark energy – dark ages, reionization, first stars – intergalactic medium – large-scale structure of Universe

1 INTRODUCTION

Cosmology has advanced at a rapid pace in recent decades, yet some major uncertainties remain. Among the most critical within the Λ CDM model are the nature of dark matter and dark energy, which together comprise approximately 95 percent of the Universe (Planck Collaboration et al. 2020). Over the past two decades, the Lyman- α forest (Ly α) has solidified itself as the current primary cosmological probe of the Universe in the $2 \lesssim z \lesssim 4$ range (McDonald et al. 2000; Croft et al. 2002). It has contributed to advances in our understanding of dark matter (Viel et al. 2005; Yèche et al. 2017; Palanque-Delabrouille et al. 2020) and dark energy (Alam et al. 2021; DESI Collaboration et al. 2024b), further cementing its role in modern cosmological studies.

The Ly α forest is composed of a series of absorption troughs occurring blueward of the Ly α emission peak in the emitted radiation of high-redshift background quasars (for a review, see Rauch 1998). These absorption features arise from neutral hydrogen clouds in the intergalactic medium (IGM), which absorb Ly α radiation in their rest frames. Since these clouds trace the underlying dark matter distribution, the Ly α forest is then a biased tracer of the total matter distribution in the post-reionization era (Viel et al. 2004; Chabanier et al. 2019). However, the forest’s sensitivity to the thermal state of the IGM – primarily through the abundance of neutral hydrogen –

makes it susceptible to astrophysical systematics that can modify the thermal evolution of the IGM at $z > 2$.

Typically, the thermal evolution of the IGM is modeled by a tight temperature-density relation, expressed as a power law $T = T_0 \Delta^{\gamma-1}$, where T_0 and γ are free parameters (Hui & Gnedin 1997). This relation arises as a consequence of the scaling of the recombination rate with temperature, and it is facilitated by both adiabatic expansion and Compton cooling (McQuinn & Upton Sanderbeck 2016)¹. For cosmological parameter inference, these thermal parameters must be marginalized over to account for uncertainties in the IGM’s thermal state (e.g., Chabanier et al. 2019).

The Dark Energy Spectroscopic Instrument (DESI; Abareshi et al. 2022) is already transforming the landscape of observational cosmology (DESI Collaboration et al. 2023b,a), providing the astrophysics community with valuable Ly α spectra for Baryon Acoustic Oscillations (BAO) studies and highly-anticipated broadband analyses (Valluri et al. 2022). Conservatively, the Ly α forest can be used to measure the scale of the BAO signal (e.g., du Mas des Bourboux et al. 2020; DESI Collaboration et al. 2024a), usually by separating the analysis into a peak and a smooth component for the correlation function (e.g., Font-Ribera et al. 2014). Optimistically, the forest offers a wealth of additional cosmological information than just the BAO standard ruler (Cuceu et al. 2021; Montero-Camacho & Mao

* E-mail: pmontero@pcl.ac.cn (PMC)

† E-mail: ymao@tsinghua.edu.cn (YM)

¹ Also, see Wells et al. (2024) for the predominant role of the neutral hydrogen fraction on the temperature-density relation.

2021; Saha et al. 2024) but so far limited access to shape information beyond the one-dimensional Ly α power spectrum has been achieved².

Regardless of the desired observational program, to accurately model the Ly α forest, several astrophysical and instrumental systematics need to be taken care of. For example, spectra with broad absorption lines (Guo & Martini 2019; Ennesser et al. 2022; Ángela García et al. 2023; Filbert et al. 2023), continuum fitting (Lee et al. 2012; Sun et al. 2023), spectra with damped Ly α systems (Parks et al. 2018; Ho et al. 2021; Wang et al. 2022), relativistic effects (Iršič et al. 2016; Lepori et al. 2020), relics from H I reionization (Montero-Camacho et al. 2019; Wu et al. 2019; Molaro et al. 2022) and He II reionization (Compostella et al. 2013; La Plante et al. 2017; Upton Sanderbeck & Bird 2020), self-shielding of minihalos (Park et al. 2023), and UV clustering (Pontzen 2014; Gontcho A Gontcho et al. 2014; Tie et al. 2019; Long & Hirata 2023). Moreover, instrumental systematics such as fiber collisions and sky residuals (Guy et al. 2024) also need to be corrected.

Recent efforts have focused on using the Ly α forest as much more than just a BAO probe, recovering some of the 3D shape information in the correlation function (e.g., Cuceu et al. 2021, 2022a), and highlighted the potential gains by combining the Alcock-Paczyński effect (Alcock & Paczynski 1979) and BAO for cosmological analysis of the Ly α correlation function (Cuceu et al. 2022b; Gerardi et al. 2023). However, access to the information stored in the broadband shape of the correlation function does not come for free. The main advantage of BAO analysis is that contaminating the location of the peak is difficult since the contaminant must rely on physical effects that have a preferred scale that aligns with the BAO (e.g., Hirata 2018; Givans & Hirata 2020). However, broadband cosmological information does not have the same protection. In particular, the Alcock-Paczyński effect, for instance, can cause an increase or decrease in the amplitude of the monopole of the correlation function, which could be confused with the effect of H I reionization relics (see Figure 4 of Montero-Camacho et al. 2023).

In this work, we explore an effect that can introduce broadband contamination to the Ly α forest correlation function, namely the imprints of cosmic reionization that leave lasting relics in the post-reionization IGM, i.e. the so-called *memory of H I reionization*. This effect leads to the breakdown of the temperature-density relation as a good approximation in the redshift range $2 < z < 4$ (Hirata 2018; Montero-Camacho et al. 2019; Montero-Camacho & Mao 2020). As shown by Montero-Camacho et al. (2023), the reionization relics do change the broadband shape of the correlation function multipoles significantly, particularly at high redshifts. In contrast, the effect is diminished at lower redshift since the IGM has more time to relax the additional injected energy during the reionization process and to get closer to recovering the temperature-density power law.

X-ray preheating of the IGM before reionization likely diminishes the imprint of reionization relics in the Ly α forest at redshifts near the quasar luminosity peak ($z \sim 2$). However, at higher redshifts, it will strengthen the impact of reionization in the IGM (Montero-Camacho et al. 2024b). Despite uncertainties surrounding the sources of X-ray preheating, its lasting influence in the post-reionization IGM offers a new avenue to constrain the astrophysics that governs the X-ray sources during cosmic dawn. Furthermore, while the high-redshift Ly α forest has often been shown to be a promising tool for constraining the nature of dark matter, particularly warm dark

matter (Palanque-Delabrouille et al. 2020; Zhang et al. *in prep.*), this potential is somewhat tempered by the strong impact of the reionization relics in this regime (Garzilli et al. 2021).

The rest of this paper is organized as follows. We describe the data used throughout this work in §2. In §3, we introduce the ingredients necessary to model the correlations of the Ly α forest. In particular, two distinct methodologies to account for the memory of reionization in the IGM are described in §3.5. In §4, we describe our findings and compare them with the original extended Baryonic Oscillation Spectroscopic Survey (eBOSS) Data Release 16 (DR16) analysis (du Mas des Bourboux et al. 2020). Furthermore, we establish the impact of reionization relics in the Ly α forest correlation functions and the inferred model parameters in §4.2. §5 discusses some caveats of our strategy. Finally, we summarize our findings in §6. In Appendix A, we introduce the parameter values of our Yukawa reionization model. We show the equivalency of our reionization approaches in Appendix B, while Appendix C presents an alternative reionization model allowed to span reionization timelines beyond those covered in our reionization simulations.

Unless otherwise specified, a flat- Λ CDM cosmology from Planck Collaboration et al. (2016) is adopted, with $\Omega_m = 0.31457$, $\Omega_b = 0.049$, and $h = 0.6731$. Other relevant derived parameters are shown in §4 and Table 2 of du Mas des Bourboux et al. (2020).

2 DATA

Throughout this work, we utilize the publicly available³ quasar catalog from the eBOSS DR16 (Lyke et al. 2020). Here we briefly describe the catalog and measurements but refer interested readers to the main eBOSS DR 16 analysis for details (du Mas des Bourboux et al. 2020).

This catalog contains more than 480,000 quasars within the redshift range $0.8 < z < 2.2$ and over 239,000 quasars for the Ly α forest measurements. In comparison, the early data release from the Dark Energy Spectroscopic Instrument (DESI; DESI Collaboration et al. 2022) includes a total of 318,691 quasars between the early data release and two months of the main survey (Ramírez-Pérez et al. 2024) while the DESI Year 1 Ly α BAO analysis has 1,529,530 quasars in total with 709,565 at $z > 1.77$ (DESI Collaboration et al. 2024a).

In this work, we analyze Ly α absorption in two spectral regions. The “Ly α ” region spans the rest-frame wavelength range $104 < \lambda_{\text{RF}} < 120$ nm, lying between the quasar Ly α and Ly β – OVI emission peaks. The “Ly β ” region covers $92 < \lambda_{\text{RF}} < 102$ nm, extending from the Ly β – OVI emission peak to the quasar rest-frame Lyman limit (du Mas des Bourboux et al. 2020). The Ly β region is affected by absorption from higher-order Lyman lines, necessitating the separation of the forests for an accurate analysis.

With the eBOSS DR 16, one can construct the following correlation functions⁴:

- Ly α (Ly α) \times Ly α (Ly α)
- Ly α (Ly α) \times Ly α (Ly β)
- Ly α (Ly α) \times quasar
- Ly α (Ly β) \times quasar

³ https://www.sdss4.org/dr16/algorithms/qso_catalog

⁴ There are two extra correlations that one could compute with this data, namely quasar auto-correlation and the auto-correlation of Ly α fluctuations in the Ly β region, i.e. Ly α (Ly β) \times Ly α (Ly β). However, we follow the eBOSS analysis and focus on the four correlations with higher signal to noise.

² See Abdul Karim et al. (2024); de Belsunce et al. (2024) for recent efforts aimed at unlocking the three-dimensional Ly α forest power spectrum.

We refer to the Ly α absorption in the Ly α region as Ly α (Ly α), while Ly α (Ly β) corresponds to Ly α absorption in the Ly β region.

In terms of observed wavelength, the eBOSS data used in this paper covers the range $\lambda \in [3600, 6000] \text{ \AA}$, where the upper limit is set by the focus on quasars with redshifts $z_q < 4$. The lower limit is caused by the high atmospheric absorption in the ultraviolet.

Furthermore, damped Lyman- α absorbers (DLA) and broad absorption line (BAL) troughs were identified in the quasar spectra as described in Lyke et al. (2020) following a similar procedure to that of Guo & Martini (2019) for BALs and using a neural network for DLAs (Parks et al. 2018).

The four correlation functions are computed using comoving separation bins (r_{\parallel}, r_{\perp}) adopting the Λ CDM cosmology of Planck Collaboration et al. (2016) to convert angular and redshift separations into physical distances. This strategy is well-motivated, as the BAO scale remains relatively stable across redshifts, even when the fiducial cosmology deviates significantly from the true cosmology (Cuceu et al. 2024). Although reionization can influence the fiducial cosmology (Montero-Camacho et al. 2024a), its effects are unlikely to disrupt this stability. The auto-correlation functions are computed using comoving separation bins of length $4 h^{-1} \text{ Mpc}$ along both parallel and perpendicular directions, resulting in a total of 2500 bins (covering $r_{\parallel}, r_{\perp} \in [0, 200] h^{-1} \text{ Mpc}$). In contrast, the cross-correlation functions are asymmetric under the permutation of the two tracers. Thus, the cross-correlations have $r_{\parallel} \in [-200, 200] h^{-1} \text{ Mpc}$ and utilize a total of 5000 bins.

For further details regarding the computation of the correlation functions and covariance matrix from the data we refer the readers to §3 of du Mas des Bourboux et al. (2020). Compared to recent analyses, such as DESI Collaboration et al. (2024a), the approach of du Mas des Bourboux et al. (2020) for the covariance matrices computes each covariance of the four correlation functions in isolation, i.e. ignoring the cross-covariances between them. This can lead to $\sim 10\%$ underestimation of the uncertainties on the BAO parameters (DESI Collaboration et al. 2024a) and should also affect other non-BAO parameters.

Figure 1 displays the measurement of the Ly α forest auto-correlation using Ly α pixels from the Ly α region, for orientations that are farther from the line-of-sight (LOS) with $0 < \mu < 0.5$, where μ is the cosine of the angle between the pixel pairs and the LOS. While the correlation function is measured over the full range $r_{\parallel}, r_{\perp} \in [0, 200] h^{-1} \text{ Mpc}$, the fits are restricted to separations $r \in [10, 180] h^{-1} \text{ Mpc}$, with $\mu \in [0, 1]$ for auto-correlations and $\mu \in [-1, 1]$ for cross-correlations. The fitting uses 1590 bins for each of the auto-correlations and 3180 bins for each of the cross-correlations. Hence, the combined analysis, encompassing two auto-correlation and two cross-correlations, involves a total of 9540 bins.

3 MODEL

Our base model largely follows the methodology of Gordon et al. (2023) and du Mas des Bourboux et al. (2020) (and references therein), taking full advantage of picca (du Mas des Bourboux et al. 2021), a python package developed for IGM cosmological-correlation analyses. Furthermore, we closely follow the picca tutorial for reproducing the eBOSS DR16 analysis outside of NERSC⁵. This section outlines the primary physical ingredients of the base

model but we refer interested readers to the previously mentioned works. In essence, the model for the Ly α forest and its cross-correlation with quasars needs the following ingredients: biases, including the redshift-space distortion parameters (RSD), and their redshift evolution (§3.1), quasilinear power spectrum (separated into peak and smooth components), which is needed for the BAO extraction (§3.2), nonlinear corrections (§3.3), and a term to account for the binning of the data (§3.4). Moreover, we include contamination due to high-column-density (HCD) systems (§3.6), quasar radiation effects and quasar redshift errors (§3.7), metals (§3.8), instrumental systematics (§3.9), and continuum distortions (§3.10). Beyond the *conventional* modeling, we incorporate, for the first time, the long-term impact of inhomogeneous reionization on the Ly α forest in the cosmological analysis of Ly α forest data (§3.5; Montero-Camacho et al. 2019).

The base model for the auto-Ly α and cross Ly $\alpha \times$ quasar power spectra, excluding the impact of inhomogeneous reionization, can be written as

$$P_{ab}(k, \mu_k, z) = b_a(z)b_b(z)(1 + \beta_a\mu_k^2)(1 + \beta_b\mu_k^2) \times P_{\text{QL}}(k, \mu_k, z)F_{\text{NL}}(k, \mu_k)G(k, \mu_k), \quad (1)$$

where b_a and β_a are the bias and RSD parameter of tracer a , respectively, and the similar notation convention applies to the tracer b . Here $\mu_k = k_{\parallel}/k$ is the cosine of the angle between the mode \mathbf{k} and the LOS, P_{QL} contains the matter power spectrum, F_{NL} is the nonlinear correction, and G is the grid term.

3.1 Bias factors and RSD parameters

We measure the BAO parameters at an effective redshift $z_{\text{eff}} = 2.334$ (du Mas des Bourboux et al. 2020). To account for redshift evolution, we adopt the following parametrizations (McDonald et al. 2006; du Mas des Bourboux et al. 2019)

$$b_{\text{F}}(z) = b_{\text{F}}(z_{\text{eff}}) \left(\frac{1+z}{1+z_{\text{eff}}} \right)^{2.9}, \quad (2)$$

$$b_{\text{q}}(z) = 3.60 \left(\frac{1+z}{1+z_{\text{eff}}} \right)^{1.44}. \quad (3)$$

For consistency with previous Ly α BAO analyses (du Mas des Bourboux et al. 2020; Gordon et al. 2023), we assume that the RSD parameters – β_{F} and β_{q} – do not evolve with redshift.

In total, we introduce three free parameters to model the Ly α forest and QSO RSD and bias factors. However, for analyses relying solely on cross-correlation data, we fix the QSO RSD parameter $\beta_{\text{q}} = 0.2602$, as was done in the eBOSS DR16 analysis. This choice is justified by the limited constraining power of the dataset in such cases. Likewise, the choice of fixed QSO bias is justified since the cross-correlation is only sensitive to the product of the quasar and Ly α biases.

3.2 Quasi-linear matter power spectrum

In order to facilitate the extraction of the BAO parameters, we decompose the matter power spectrum into a peak component and a smooth component, incorporating nonlinear broadening corrections,

$$P_{\text{m}}^{\text{QL}}(\mathbf{k}, z) = P_{\text{m}}^{\text{peak}}(\mathbf{k}, z) \exp\left(-\frac{k_{\parallel}^2 \Sigma_{\parallel}^2 + k_{\perp}^2 \Sigma_{\perp}^2}{2}\right) + P_{\text{m}}^{\text{smooth}}(\mathbf{k}, z), \quad (4)$$

⁵ Available at https://github.com/igmhub/picca/blob/master/tutorials/eboss_dr16/tutorial_instructions.ipynb

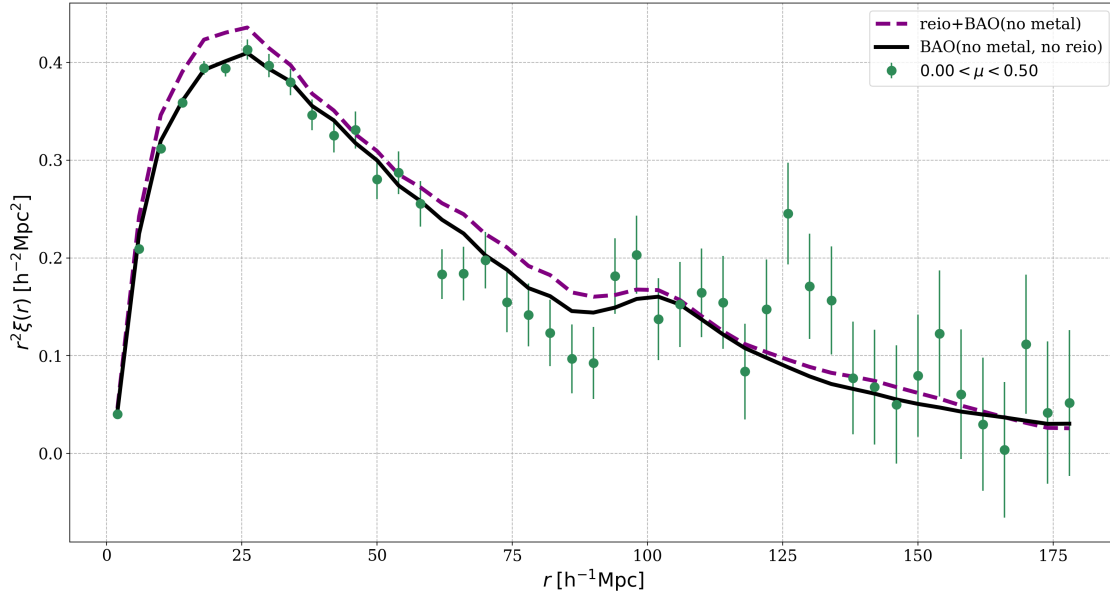


Figure 1. Wedge plot of the Ly α (Ly α) auto correlation function for $0.00 < \mu < 0.50$. The green points represent the eBOSS DR16 data. The black solid curve illustrates the auto-correlation function without metal contamination, highlighting the contribution of the BAO peak. The purple dashed curve includes the impact of reionization but does not correspond to the best fit; it is shown to demonstrate the broadband impact of reionization and it corresponds to the PySR late reionization scenario which gives the strongest deviations relative to the fiducial no reionization model (see §3.5 for a description of the reionization scenarios considered throughout this work). To clearly isolate the influence of reionization relics, metal contamination is removed from the plotted correlation functions, as metal absorption introduces additional features along the LOS, notable a prominent bump around $r_{\parallel} \approx 111 h^{-1} \text{Mpc}$, which overlaps with the BAO peak (see Figure 7 in Gordon et al. 2023).

where $\Sigma_{\parallel} = 6.42 h^{-1} \text{Mpc}$ and $\Sigma_{\perp} = 3.26 h^{-1} \text{Mpc}$ are the nonlinear broadening scales of the BAO peak (Eisenstein et al. 2007). Note that only $P_{\text{m}}^{\text{peak}}$ contains BAO information.

The decomposition is achieved using the sideband technique detailed in Kirkby et al. (2013). This method involves transforming the linear matter power spectrum into correlation function through Fourier transformation and two sidebands are defined surrounding the BAO feature. A smooth function is fitted to connect these sidebands, effectively removing the BAO feature from the correlation function. The resulting smooth correlation function is then transformed back to k -space, yielding $P_{\text{m}}^{\text{smooth}}$. Consequently, the peak power spectrum is given by $P_{\text{m}}^{\text{peak}} = P_{\text{m}}^{\text{L}} - P_{\text{m}}^{\text{smooth}}$.

3.3 Nonlinear correction

Even though the BAO feature is a large-scale phenomenon, accurately modeling systematics in the correlation functions requires sensitivity to smaller separations, scales below $80 h^{-1} \text{Mpc}$, which are not strictly necessary to detect the BAO signal. The main reason for carefully addressing these smaller scales is that the observed transmitted flux fluctuations δ_{F} can be distorted by the distortion matrix (see §3.10), effectively propagating some of the small-scale nuisance into larger separations.

The nonlinear correction for the auto-correlation is given by (Arinyo-i-Prats et al. 2015)

$$\ln F_{\text{NL}}^{\text{auto}}(\mathbf{k}, z_{\text{eff}}) = q_1 \Delta_{\text{L}}^2(k, z_{\text{eff}}) \left[1 - \left(\frac{k}{k_{\text{v}}} \right)^{a_{\text{v}}} |\mu_{\text{k}}|^{b_{\text{v}}} \right] - \left(\frac{k}{k_{\text{p}}} \right)^2, \quad (5)$$

where $\Delta_{\text{L}}^2 \equiv k^3 P_{\text{L}} / (2\pi^2)$ and with the remaining parameter values interpolated to z_{eff} using Table 7 of Arinyo-i-Prats et al. (2015). The first term in Eq. (5) corresponds to the expected isotropic nonlinear enhancement of the power spectrum, where q_1 is dimensionless and controls the importance of this nonlinear enhancement. The second term accounts for the suppression along the LOS due to peculiar velocities, the parameter k_{v} is the characteristic wave number of the velocity broadening effect, while a_{v} and b_{v} are the power law exponents controlling the velocity broadening effect as a function of k and μ respectively. The third term represents the isotropic suppression caused by gas pressure below the Jeans scale, where k_{p} is related to the temperature-density relationship of the IGM and plays a role similar to Jeans scale. (It is not a strict physical Jeans scale, but an empirical parameter determined by fitting).

We emphasize that Eq. (5) is evaluated at the effective redshift, which introduces a minor approximation. Specifically, this procedure neglects some small variation in the nonlinear parameters due to different $(r_{\parallel}, r_{\perp})$ -bins having mean redshifts that vary over the range $2.32 \lesssim \bar{z} \lesssim 2.39$ (du Mas des Bourboux et al. 2020).

For the cross-correlation, we account for the effects of redshift errors and quasar nonlinear velocities (Percival & White 2009), which smear the signal along the LOS. We correct for these effects using

$$F_{\text{NL}}^{\text{cross}}(k_{\parallel}) = \frac{1}{\sqrt{1 + k_{\parallel}^2 \sigma_{\text{v}}^2}}, \quad (6)$$

where σ_{v} is a free parameter that must be marginalized over to extract BAO parameters. σ_{v} encapsulates the smoothing induced by redshift

uncertainties. Note that the auto-correlation function is also affected by statistical redshift errors (Youles et al. 2022).

3.4 Grid-binning term

To account for the effect of binning the correlation functions into a $(r_{\parallel}, r_{\perp})$ -grid, we introduce a grid term. We assume a uniform distribution within each bin, which is a sufficiently accurate approximation (Bautista et al. 2017). The grid term G can be written as the product of two top-hat functions

$$G(\mathbf{k}) = \text{sinc}\left(\frac{k_{\parallel}R_{\parallel}}{2}\right) \text{sinc}\left(\frac{k_{\perp}R_{\perp}}{2}\right), \quad (7)$$

where $R_{\parallel} = R_{\perp} = 4 h^{-1}$ Mpc are the bin widths in the radial and transverse directions, respectively.

3.5 Imprints from H I reionization

Ultraviolet heating during reionization raises the temperature of the IGM to $\mathcal{O}(10^4)$ K; however, underdense gas within minivoids can also undergo shock heating and compression to mean density due to shocks propagating from surrounding denser regions (Hirata 2018). Consequently, the commonly assumed temperature-density relation, $T = T_0 \Delta^{\gamma-1}$ (Hui & Gnedin 1997), becomes bimodal. This new phase, referred to as the high-entropy mean-density (HEMD) mode, reaches a higher adiabat and traces the denser gas in its evolution. The relaxation of the excess energy deposited during reionization occurs over cosmological timescales, with the HEMD gas eventually converging back to the standard temperature-density relation by $z \sim 2$ (Hirata 2018; Montero-Camacho & Mao 2020).

Furthermore, reionization proceeds in an inhomogeneous manner, with denser regions ionizing earlier due to the proximity of ultraviolet radiation sources. Therefore, the reionization process does not occur simultaneously across all regions, leading to spatial variations in the strength and timing of reionization. These inhomogeneities imprint distinct signatures on cosmological observables of the post-reionization era (Long et al. 2023; Montero-Camacho et al. 2025), which couple with the spatial scale of ionized bubbles, typically ranging from $\sim 1 - 10$ Mpc (Montero-Camacho et al. 2019).

These long-lasting relics of reionization are inherently sensitive to the astrophysical processes governing cosmic reionization, presenting a valuable and novel avenue for constraining the reionization timeline (Montero-Camacho & Mao 2021). Likewise, they provide insights into the era of cosmic dawn (Montero-Camacho et al. 2024b), particularly regarding X-ray preheating, offering the potential to deepen our understanding of the nature and sources of X-rays in the early Universe. Conversely, neglecting the impact of reionization relics can result in significant biases and an underestimation of uncertainties when inferring cosmological parameters from the Ly α forest (Montero-Camacho et al. 2023).

The memory of reionization in the Ly α forest, i.e. the impact of inhomogeneous reionization in the post-reionization Ly α forest, is given by (Montero-Camacho et al. 2019)

$$P_{\text{F}}(\mathbf{k}, z) = b_{\text{F}}^2(z)(1 + \beta_{\text{F}}\mu_k^2)^2 P_{\text{m}}(k, z) F_{\text{NL}}(\mathbf{k}, z) G(\mathbf{k}) + 2b_{\text{F}}(z)b_{\Gamma}(z)(1 + \beta_{\text{F}}\mu_k^2) P_{\text{m},\psi}(k, z) G(\mathbf{k}), \quad (8)$$

where we include the grid correction term G and b_{Γ} is the radiation bias (Arinyo-i-Prats et al. 2015; Hirata 2018). The term $P_{\text{m},\psi}$ corresponds to the cross-power spectrum between matter and transparency of the IGM. This cross-power spectrum captures the effect of

reionization through its effect on the optical depth and the spatial distributions of ionized regions. A detailed derivation of this formalism is provided in §2 of Montero-Camacho et al. (2019).

Accurately modeling the effects of inhomogeneous reionization on the Ly α forest within the redshift range $2 < z < 4$ poses significant computational challenges. Simulations must resolve the complex interactions between small-scale structure and reionization with sufficient mass resolution to capture processes occurring below the Jeans mass prior to the passage of an ionization front (Montero-Camacho & Mao 2020). Moreover, the patchy nature of reionization requires tracking spatial variations across large scales to achieve the necessary statistical power. Consequently, the simulations needed to capture these physical processes and to model the Ly α forest demand a computationally expensive huge dynamical range. To circumvent these computational demands, we adopt the analytical approach introduced by Montero-Camacho et al. (2023) to approximate the effects of reionization relics in the post-reionization IGM. This model employs a Yukawa-like template with three free, redshift-dependent parameters, and it is given by

$$P_{\text{m},\psi}(k, z) = -\frac{A_{\text{re}}(z)}{(k/k_0)\beta_{\text{re}}(z)} e^{-\alpha_{\text{re}}(z)(k/k_0)} [\text{Mpc}^3], \quad (9)$$

where $k_0 = 1 \text{ Mpc}^{-1}$, A_{re} corresponds to the amplitude of the cross-power spectrum, α_{re} represents a screening coefficient, and β_{re} corrects for the large scale shape of the memory of reionization. These parameters are determined from simulation fits and interpolated to z_{eff} . Table A1 in Appendix A tabulates the values of the template parameters for different reionization scenarios at z_{eff} .

As demonstrated in Figure 3 of Montero-Camacho et al. (2023), Eq. (9) performs remarkably well at large scales but its performance worsens for $k \gtrsim 0.4 \text{ Mpc}^{-1}$. This limitation arises from the difficulty of the analytic template to fully capture the interplay between small-scale structure and reionization relics. Given the significant uncertainties in the reionization timeline (e.g. Morales et al. 2021) and the complexities in the epoch of reionization modeling (see, for example, Park et al. 2019), the adopted Yukawa-like template provides sufficient robustness for the scope of this study. Notably, for a known reionization history, this template methodology has shown efficacy in reproducing the multipoles of the Ly α auto-correlation function (see Figure 5 of Montero-Camacho et al. 2023). However, to mitigate the declining performance at smaller scales from compromising the Ly α model, we truncate the impact of reionization by setting it to zero for $k > 0.4 \text{ Mpc}^{-1}$. This truncation is justified as reionization relics rapidly diminish with increasing wavenumber, as illustrated in Figure 3 of Montero-Camacho & Mao (2020).

Likewise, Eq. (9) is valid for $k_{\text{min}} \approx 0.06 \text{ Mpc}^{-1}$ due to the finite box size of the simulations used to derive this template. To model larger scales ($k < k_{\text{min}}$), we adopt a linear biasing as follows

$$P_{\text{m},\psi}(k < k_{\text{min}}, z_{\text{eff}}) = \frac{P_{\text{m},\psi}(k_{\text{min}}, z_{\text{eff}})}{P_{\text{m}}^{\text{L}}(k_{\text{min}}, z_{\text{eff}})} P_{\text{m}}^{\text{L}}(k, z_{\text{eff}}). \quad (10)$$

This approach should provide sufficient accuracy for scales larger than the typical ionized bubble size. Nevertheless, we emphasize the importance of exploring larger simulation volumes in preparation for the scales DESI will probe with the 1D flux power spectrum (Ravoux et al. 2023; Ramírez-Pérez et al. 2024).

As an alternative to the analytical Yukawa-like template for describing the memory of reionization in the Lyman- α forest, and to facilitate its application to 1D Ly α flux power spectrum measurements, we propose an additional expression valid for a Planck-like reionization. This new template is derived using PySR (Cranmer

et al. 2020)⁶, a Python package designed for high-performance Symbolic Regression, utilizing a JULIA backend. Symbolic regression, as implemented in PySR, provides an efficient methodology for discovering interpretable mathematical expressions that best describe complex datasets (see e.g. Udrescu & Tegmark 2020, for more details regarding symbolic regression). For this work, the symbolic regression algorithm was trained on the same dataset used to derive the Yukawa-like template, specifically the *bubble* models of Montero-Camacho & Mao (2020). To enhance interpretability and physical relevance, we introduce a series of constraints during the training process. The exponential operator was preferentially weighted over binary operators, such as addition and subtraction. Furthermore, power-law terms (x^y) were limited in complexity, allowing y to be either a constant or a single-variable factor. Exponential terms were restricted to arguments of limited complexity, capped at four instances of variables or variable-constant combinations – e.g., e^{x^4} and e^{ax} are allowed, whereas nested forms like e^{e^x} are excluded. The training data included wavenumber and redshift as the only independent variables. For further technical details on the derivation and implementation of the PySR templates, we refer readers to Montero-Camacho (prep).

Under these constraints, and given the simulation data, we obtain the following expression for the memory of reionization in the Ly α forest power spectrum

$$P_{m,\psi}(k, z) = -0.307 \left(\frac{11.9z}{z^{5.86}} \right) \left(\frac{e^{-2.04(k/k_0)}}{(k/k_0)^{2.04}} \right) [\text{Mpc}^3], \quad (11)$$

with $k_0 = 1 \text{ Mpc}^{-1}$.

Eq. (11) preserves the Yukawa-like structure of the Yukawa-like template. While a comprehensive and quantitative evaluation of Eq. (11) — the theme of a future companion paper — is beyond the scope of this paper, Appendix B offers a comparative analysis of its performance relative to the original Yukawa-like template for the purpose of this work. The PySR template has the same domain of validity as Eq. (9), requiring the adoption of analogous strategies to handle the boundary conditions. Specifically, for $k > 0.4 \text{ Mpc}^{-1}$, we set the contribution from reionization to zero due to its rapid decline at these scales. Similarly, for $k < 0.06 \text{ Mpc}^{-1}$, we employ the linear biasing model described in Eq. (10) to address the limitations arising from the finite box size of the simulation data.

The cross-correlation between Ly α forest and quasars is also influenced by cosmic reionization. Besides its impact in the Ly α forest, reionization can potentially influence the quasars directly through the imprints it leaves in the denser regions of the IGM during the post-reionization era (Long et al. 2023). However, these effects primarily impact regions characterized by shallow potential wells during reionization, which are unlikely to represent the typical environments surrounding observed quasars. Furthermore, halos with initially shallow potential wells are expected to have recovered from the baryonic modulation induced by reionization by $z \approx 3.5$. Consequently, the cross-power spectrum – including reionization relics – can be written as

$$P_{\text{cross}}(\mathbf{k}, z) = b_{\text{F}} b_{\text{q}} (1 + \beta_{\text{F}} \mu_k^2) (1 + \beta_{\text{q}} \mu_k^2) P_{\text{m}} F_{\text{NL}}^{\text{cross}} G + b_{\text{q}} b_{\Gamma} (1 + \beta_{\text{q}} \mu_k^2) P_{m,\psi} G. \quad (12)$$

The relics of reionization naturally depend on the timeline of cosmic reionization, as a more recent reionization would allow less time for the IGM to relax the additional energy injected during this epoch. To explore this dependency, we consider three distinct reionization

scenarios: early, mid, and late reionization. The mid reionization scenario assumes a neutral hydrogen evolution consistent with Planck Collaboration et al. (2020), while the early and late scenarios are designated to be approximately consistent with Planck’s 1σ errors on the inferred reionization timeline. Our terminology is that the Yukawa template with early reionization is referred to as “Yukawa early”, whereas “PySR late” corresponds to the symbolic regression template with the late reionization scenario. Eq. (11) corresponds to the PySR mid model, while the PySR early template has the form

$$\begin{cases} x \equiv \frac{e^{-2(k/k_0)}}{(k/k_0)^2} \\ f(z) = (-0.19956973z + 1.9220588)^z - 2.8029568 \\ P_{m,\psi}(k, z) = f(z) \cdot x^{1.0633986} [\text{Mpc}^3]. \end{cases} \quad (13)$$

For late reionization, the PySR late model is given by

$$\begin{cases} x = k/k_0 + 0.0037718469 \\ f(z) = \frac{z^{-4.6010156}}{0.13144803z} \\ P_{m,\psi}(k, z) = f(z) \cdot \frac{e^{-2x}}{-2.2932026x^2} [\text{Mpc}^3], \end{cases} \quad (14)$$

where k_0 is still 1 Mpc^{-1} . Appendix A introduces the values of A_{re} , α_{re} , and β_{re} for the Yukawa early, mid, and late templates.

All templates, including the Yukawa templates, are evaluated at the effective redshift $z_{\text{eff}} = 2.334$ when entering the correlation function model.

Appendix B presents a comparison of the two distinct methodologies employed to incorporate the memory of reionization into the Ly α forest model. Our findings demonstrate that the templates yield results that are largely equivalent. Thus, for the sake of clarity and brevity, we focus solely on the PySR-based results in the main text. However, we emphasize that the full analysis was conducted using both methodologies to ensure the robustness of the reionization modeling. Furthermore, Appendix C explores a variation of the Yukawa template, introducing an additional free parameter by allowing its amplitude A_{re} to vary. This modified Yukawa template, with one free parameter, successfully recovers BAO parameters that are consistent with the results from the other templates.

We note that both the Yukawa and PySR templates do not include the effects of X-ray preheating prior to the onset of H I reionization. The incorporation of X-ray heating during the cosmic dawn leads to a strengthening of the imprints from reionization at higher redshifts but also to a small suppression at lower redshifts ($z \sim 2$) – depending on specific X-ray prescription (Montero-Camacho et al. 2024b).

3.6 Absorption by HCD systems

In the eBOSS context, high column density (HCD) systems are defined as neutral hydrogen absorbers with column densities exceeding $10^{17.2} \text{ cm}^{-2}$ (du Mas des Bourboux et al. 2020). These systems mainly consists of Lyman limit systems and DLAs (Wang et al. 2022). An ideal Ly α forest survey would perfectly identify and mask all HCD absorption regions to remove their effect on the correlation functions. Unfortunately, in practice, this task remains challenging. Residual HCDs that go undetected introduce systematic modifications to the correlation functions, particularly along the radial direction. On large scales, this effect manifests as a broadening of the signal that introduces a dependence on k_{\parallel} for the Ly α bias and RSD

⁶ <https://github.com/MilesCranmer/PySR>

parameter as follows (Font-Ribera & Miralda-Escudé 2012)

$$\tilde{b}_F = b_F + b_{\text{HCD}} F_{\text{HCD}}(k_{\parallel}), \quad (15)$$

$$\tilde{b}_F \tilde{\beta}_F = b_F \beta_F + b_{\text{HCD}} \beta_{\text{HCD}} F_{\text{HCD}}(k_{\parallel}), \quad (16)$$

where b_{HCD} and β_{HCD} are the bias and RSD parameter associated with HCD systems, respectively. In the fit of the auto-correlation functions, these parameters are treated as free parameters, while for the cross-correlations, they are fixed to $b_{\text{HCD}} = -0.0501$ and $\beta_{\text{HCD}} = 0.703$, respectively. Moreover, F_{HCD} models the suppression effect induced by HCD systems and is defined as (Rogers et al. 2018)

$$\ln F_{\text{HCD}}(k_{\parallel}) = -L_{\text{HCD}} k_{\parallel}, \quad (17)$$

where L_{HCD} characterizes the effective scale of the suppression. For consistency with the eBOSS DR16 analysis, L_{HCD} is fixed to $10 h^{-1} \text{Mpc}^7$.

3.7 Quasar proximity effect and quasar redshift errors

The radiation emitted by a quasar can have a strong influence on its surrounding neighborhood. Assuming isotropic emission, this transverse proximity effect can be expressed as (Font-Ribera et al. 2013)

$$\xi^{\text{TP}} = \xi_0^{\text{TP}} \left(\frac{1 h^{-1} \text{Mpc}}{r} \right)^2 \exp\left(-\frac{r}{\lambda_{\text{UV}}}\right), \quad (18)$$

where λ_{UV} , representing the characteristic attenuation length, is set to $300 h^{-1} \text{Mpc}$ (Rudie et al. 2013), consistent with the eBOSS DR16 analysis. The amplitude ξ_0^{TP} is yet another free parameter of the model. However, in cases where only the cross-correlation information is used, ξ_0^{TP} is fixed to a value of 0.7386, again for consistency with the eBOSS DR16 analysis.

Another caveat for the cross-correlation analysis is the impact of quasar redshift errors, which can systematically alter the inferred separation between quasars and Ly α absorption regions (Bault et al. 2024). To address these systematic quasar redshift errors, we introduce an additional free parameter $\Delta r_{\parallel, \text{QSO}} \equiv r_{\parallel}^{\text{True}} - r_{\parallel}^{\text{Measured}}$, which accounts for potential biases in the measured redshifts. This correction mitigates asymmetries in the cross-correlation along positive and negative r_{\parallel} caused by redshift errors (Gordon et al. 2023). We remind the readers that Eq. (6), which models the smearing of the cross-correlations along the LOS, already incorporates another aspect of redshift errors by introducing the free parameter σ_v . This parameter accounts for the effects of redshift uncertainties on the velocity dispersion of quasars.

3.8 Absorption by metals

Besides the absorption features from the Ly α forest and HCD systems, the eBOSS data also captures absorption signatures from metals present in the IGM (Yang et al. 2022). This includes the cross-correlation between Ly α absorption and metal lines, as well as contributions from metal-metal correlations to the overall observed correlation functions.

We follow the methodology outlined in du Mas des Bourboux et al. (2020) to tackle the impact of metals. Specifically, we define a power

spectrum, P_{mn} , for each pair of absorber species m and n and process i similarly to the Ly α power spectrum, with two notable modifications. First, the HCD contribution is excluded. Second, since redshifts are assigned under the assumption of Ly α absorption, systematic deviations arise for metal absorbers due to the different transition lines involved. These deviations are addressed using a metal distortion matrix as established in Blomqvist et al. (2018). Specifically, we use Eq. (35) in du Mas des Bourboux et al. (2020).

In line with the eBOSS DR16 analysis, we focus on metal contamination from four silicon transitions: Si II (119 nm), Si II (119.3 nm), Si II (126 nm), and Si II (120.7 nm). The RSD parameters for these transitions are fixed to $\beta_m = 0.50$, motivated by previous measurements of the cross-correlation between the Ly α forest and DLAs (Font-Ribera et al. 2012), while the bias factors, e.g., $b_{\eta, \text{SiII}(119)}$, are allowed to vary. In addition, we include only the auto-correlation of C IV, with a fixed $\beta_{\text{CIV}} = 0.27$, consistent with previous findings (Blomqvist et al. 2018). The corresponding bias C IV factor, $b_{\eta, \text{CIV}(\text{eff})}$, is a free parameter but it is kept fixed to -4.8×10^{-3} for cross-correlation analyses (du Mas des Bourboux et al. 2020).

3.9 Instrumental systematics

The eBOSS instrument has two spectrographs, each equipped with 500 fibers, of which 450 are allocated for science observations and approximately 40 are designated as sky fibers. These sky fibers play a critical role in monitoring atmospheric conditions and are essential for performing independent sky subtraction for each spectrograph. This subtraction mitigates the Poisson fluctuations present in the sky spectra, which can induce excess correlations in bins with $r_{\parallel} = 0$. This sky-based induced correlated noise is the dominant source of contamination caused by instrumental effects in the Ly α forest observations (Guy et al. 2024).

Although this contamination initially manifests as an excess correlation at small parallel separations, continuum-fitting will propagate the distortion across all r_{\parallel} . To address this, du Mas des Bourboux et al. (2020) proposed an empirical model to fit the distortion. This model introduces two free parameters and is given by

$$\xi^{\text{sky}}(r_{\parallel}, r_{\perp}) = \begin{cases} \frac{A_{\text{sky}}}{\sigma_{\text{sky}} \sqrt{2\pi}} \exp\left(-\frac{1}{2} \left(\frac{r_{\perp}}{\sigma_{\text{sky}}}\right)^2\right), & \text{if } r_{\parallel} = 0, \\ 0, & \text{if } r_{\parallel} \neq 0, \end{cases} \quad (19)$$

where A_{sky} and σ_{sky} represent the amplitude and width of the induced correlation, respectively. Note that the contamination in the Ly α region requires one set of A_{sky} and σ_{sky} , while the Ly β region needs a separate set to account for this instrumental effect.

3.10 Continuum distortion

Fitting the quasar continua is a crucial step in determining the overall strength of absorption features in the Ly α forest. The continuum fitting procedure employed for the eBOSS DR16 analysis involves modeling the continuum for each skewer using a linear fit, characterized by an amplitude and slope (see e.g., Slosar et al. 2011). However, this method has the unintended consequence of introducing biases in both the mean and slope of flux fluctuations, which can distort the resulting correlation measurements.

To ensure a fair comparison between the model and the observed data, the physical model must be subjected to an analogous distortion. This is the responsibility of the distortion matrix D , which relates the true correlations to their distorted counterparts (Bautista et al. 2017)

$$\hat{\xi}^{\text{distorted}} = D \xi^{\text{true}}. \quad (20)$$

⁷ However, it is worth noting that the DESI Year 1 analysis allows L_{HCD} to vary, finding minimal impact on the BAO parameters (DESI Collaboration et al. 2024a). Nonetheless, variations in L_{HCD} could potentially influence the inferred bias and RSD parameters due to their intrinsic degeneracies.

Thus, the physical model of the correlations is then distorted by the distortion matrix prior to any comparison with the observed data. The specific forms of the distortion matrix for the auto-correlations and cross-correlations are detailed in Eqs. (21) and (22) of [du Mas des Bourboux et al. \(2020\)](#).

In total, the model has 13 free parameters for the $\text{Ly}\alpha(\text{Ly}\alpha)$ auto-correlation, 10 for the $\text{Ly}\alpha(\text{Ly}\alpha)$ cross-correlation, and 19 for the combined analysis of all four correlation functions. Both the reionization model and the fiducial – no reionization – model have the same number of free parameters. The determination of the two BAO parameters requires marginalizing over the remaining nuisance parameters. As such, we introduce a Yukawa template with an extra degree of freedom in Appendix C with the objective of inspecting the impact of the extra flexibility in the marginalization of nuisance parameters.

4 RESULTS

To obtain the best fit from the eBOSS $\text{Ly}\alpha$ and quasars correlation data, we follow the methodology outlined in the eBOSS DR16 tutorial available in `picca`. This approach maximizes the likelihood to determine the best-fit parameters, leveraging a Hessian matrix approach at the best-fit point to estimate uncertainties for most model parameters at the 1σ confidence level. The use of the Hessian assumes symmetric errors and is particularly effective for Gaussian-like likelihoods. Since the main cosmological product of these analyses is the BAO parameters, one then employs the MINOS⁸ algorithm from the `iminuit`⁹ minimization package to refine the determination of the 1σ confidence levels for the BAO parameters. This strategy is computationally inexpensive and well-suited for our purposes. For comparison, [du Mas des Bourboux et al. \(2020\)](#) adopted a χ^2 scan technique (detailed in their Appendix E) and derived the confidence levels for the BAO parameters using a suite of 1000 fastMC simulations of the correlation function.

4.1 No memory of reionization

To ensure the reliability of our approach, we first re-analyze the eBOSS DR16 observations using our fiducial model, following the eBOSS DR16 `picca` tutorial. The primary objective of this sanity check was to validate our implementation by reproducing the best-fit values obtained by the eBOSS collaboration. For this initial analysis, we exclude the contribution from reionization relics and focus on fitting the fiducial model.

The results of this re-analysis are presented in the first column of Table 1. A comparison with the results of [du Mas des Bourboux et al. \(2020\)](#) (see their Table 6) reveals minor deviations. For most free parameters, such as the BAO parameters and the bias and RSD parameters of the $\text{Ly}\alpha$ forest, the deviations are minimal, typically below 1%. This level of consistency demonstrates that our analysis successfully replicates the eBOSS pipeline as implemented in the `picca` tutorial. Small discrepancies, however, are expected. As noted in the tutorial, these discrepancies arise primarily due to the use of a slightly updated quasar catalog compared to the original catalog used in the eBOSS analysis. The differences are more pronounced for

the bias parameters associated with metal contaminants, where deviations can reach approximately 20%. Nevertheless, the constraining power on metal parameters is relatively weak, and the differences between our results and those of [du Mas des Bourboux et al. \(2020\)](#) remain within 1σ . Therefore, these variations are deemed acceptable for our purposes.

In Table 1, the bias parameter for the Si II (119.3 nm) line in the $\text{Ly}\alpha(\text{Ly}\alpha) \times$ quasar cross-correlation has a positive value, whereas the biases for all other metal lines are negative. Similarly, a positive bias is inferred for the Si II (119 nm) line in the $\text{Ly}\alpha(\text{Ly}\beta) \times$ quasar cross-correlation. This pattern of atypical metal bias parameters aligns with the findings of the eBOSS DR16 analysis, confirming that these results are not artifacts sourced by the `picca` tutorial. The occurrence of these positive bias signs can be attributed to statistical fluctuations, as the precision of measurements in the $\text{Ly}\beta$ region – or in the cross-correlations with quasars – is relatively limited. Consequently, the inferred biases may occasionally appear positive. However, none of the positive biases deviate by more than 2σ , indicating that these values remain statistically consistent with expectations.

Figure 1 shows the wedge plot for the $\text{Ly}\alpha(\text{Ly}\alpha)$ auto-correlation function in the range $0.00 < \mu < 0.50$. This visualization is obtained by re-binning the original $(r_{\parallel}, r_{\perp})$ rectangular grid into (r, μ) bins for visualization purposes. For clarity, the metal contamination introduced in §3.8 has been excluded from this figure. The black solid curve represents the fiducial model without a reionization term. Both the observations (green points) and the model showcase the characteristic BAO bump near $r \approx 100 h^{-1} \text{Mpc}$.

A keen reader may notice that the probability (p -value) is higher, and the corresponding χ^2_{min} is lower, for the $\text{Ly}\alpha(\text{Ly}\alpha)$ auto-correlation than for the $\text{Ly}\alpha(\text{Ly}\alpha) \times$ quasar cross-correlation. Several factors contribute to this trend. The cross-correlation includes twice the number of bins as the auto-correlation, as the former lacks symmetry under the permutation of tracers. However, the cross-correlation provides less constraining power, leading to the fixing of certain non-BAO parameters, such as $b_{\eta, \text{CIV}(\text{eff})}$ and ξ_0^{TP} , to the best-fit values reported in [du Mas des Bourboux et al. \(2020\)](#)¹⁰. As a result, the cross-correlation analysis involves 10 free parameters, while the auto-correlation uses 13.

When combining all four correlation functions, the probability decreases and the χ^2_{min} increases further. This is due to the rise in degrees of freedom (the full model uses 19 free parameters in the combined analysis) and the inclusion of less constraining datasets such as $\text{Ly}\alpha(\text{Ly}\alpha) \times \text{Ly}\alpha(\text{Ly}\beta)$ or the $\text{Ly}\alpha(\text{Ly}\beta) \times$ quasar correlations. Hence, the uneven modeling and varying constraining power of the datasets make direct comparison of p -values across different correlations unwise.

An interesting trend, also present in the recent DESI Year 1 $\text{Ly}\alpha$ BAO analysis by [DESI Collaboration et al. \(2024a\)](#), is the significantly weaker RSD parameter for quasars compared to the $\text{Ly}\alpha$ forest. Specifically, $\beta_{\text{Ly}\alpha} = 1.6641$ for the forest, compared to $\beta_{\text{q}} = 0.2593$ for quasars. These values are consistent with the DESI Year 1 results ($\beta_{\text{Ly}\alpha} \sim 1.7$, $\beta_{\text{q}} \sim 0.3$).

4.2 Impact of reionization relics on the BAO analysis

After successfully reproducing the eBOSS DR16 analysis with the fiducial model, we incorporate the effects of reionization in the $\text{Ly}\alpha$

⁸ <https://github.com/scikit-hep/iminuit/blob/develop/src/minos.cpp>

⁹ <https://github.com/scikit-hep/iminuit>

¹⁰ The best-fit values reported in the eBOSS DR16 analysis show only minor discrepancies with those obtained from our combined analysis for the no-reionization model.

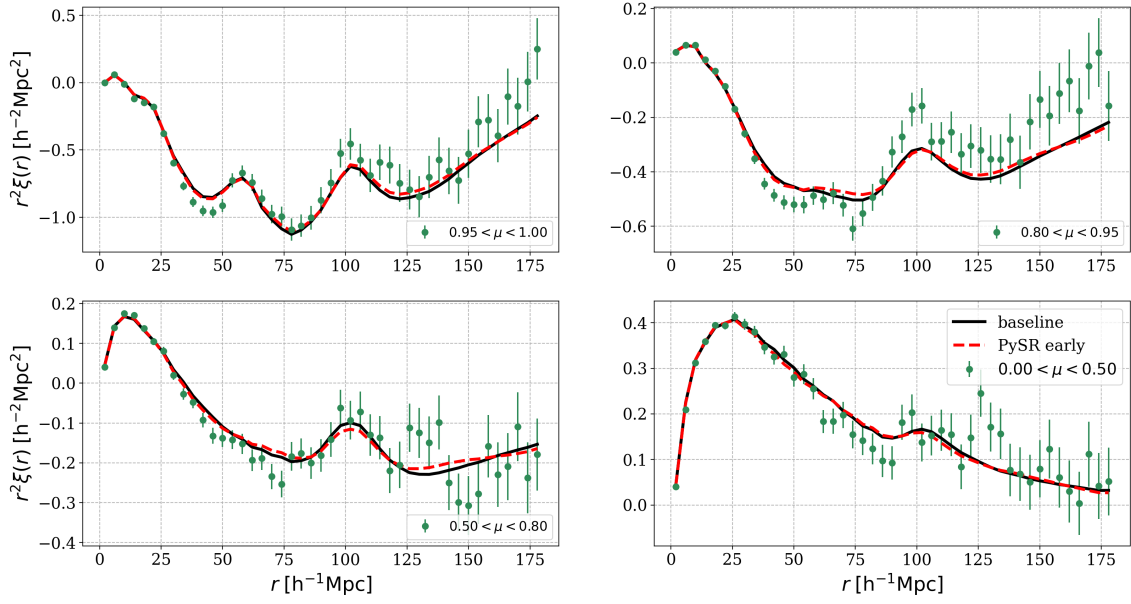


Figure 2. Wedges of the Ly α (Ly α) auto-correlation function of the Ly α forest. The black solid curve corresponds to the best-fit model for the fiducial scenario, which assumes no reionization relics. The red dashed curve represents the early reionization scenario described by the PySR early template, our best performing model. Green points correspond to the measurements from eBOSS DR16. All models include metal contamination, which explains the bumps in the top-left panel at separations of 20, 60, and 111 h^{-1} Mpc, arising from correlations with Si II and Si III (see §3.8 and Gordon et al. 2023).

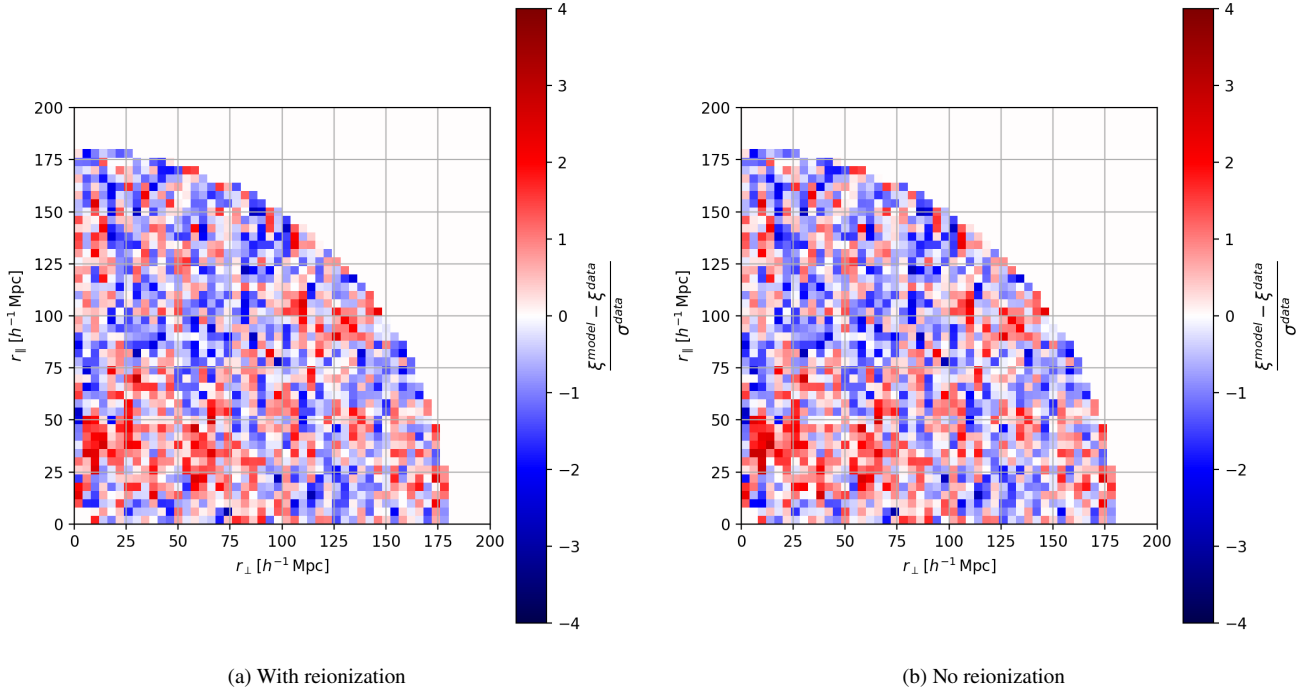


Figure 3. Residuals of the 3D Ly α (Ly α) auto-correlation function. The residuals are defined as the difference between the model and the observed data, normalized by the observational uncertainties, i.e. $(\xi^{\text{model}} - \xi^{\text{data}}) / \sigma^{\text{data}}$. In Figure 3a, the model incorporates reionization relics, as described by Eq. (8), while Figure 3b represents the fiducial scenario, which excludes reionization effects. While differences between these models appear subtle, they are sufficiently significant to bias the non-BAO parameters in the fit. See Figure 4 for highlight of the difference between the two models.

Table 1. Best-fit parameters for the auto-correlation function of the Ly α forest (from the Ly α region), the cross-correlation between the forest and quasars, and the combination of all the four correlations (including Ly α absorption in the Ly β region). We include a reference model that ignores reionization relics, alongside three variants that incorporate the impact of reionization relics in the post-reionization IGM, allowing for exploration of different reionization timelines. The gray-shaded entries identify the model that provides the best fit to the corresponding eBOSS DR16 measurements. Except for the p -value and minimum χ^2 , parameters without error bars are fixed in the fit. Unlike the original eBOSS DR16 analysis (du Mas des Bourboux et al. 2020), which reports error bars on the BAO parameters derived from 1000 fastMC realizations, the error bars for all parameters in our table are computed using the `MINUIT` package.

Parameter	No reionization	PySR early	PySR mid	PySR late
Ly α auto-correlation				
Prob.	0.285	0.328	0.327	0.317
χ^2_{\min}	1608.49	1601.41	1601.58	1603.23
α_{\parallel}	1.0458 ± 0.0339	1.0256 ± 0.0372	1.0156 ± 0.0397	1.0085 ± 0.0405
α_{\perp}	0.9814 ± 0.0422	0.9913 ± 0.0487	1.0007 ± 0.0467	1.0069 ± 0.0452
$\beta_{\text{Ly}\alpha}$	1.6331 ± 0.0864	1.7221 ± 0.0943	1.7711 ± 0.0986	1.8180 ± 0.1028
$b_{\text{Ly}\alpha}$	-0.1187 ± 0.0023	-0.1131 ± 0.0022	-0.1103 ± 0.0021	-0.1079 ± 0.0021
$b_{\eta, \text{Ly}\alpha}$	-0.1998 ± 0.0039	-0.2007 ± 0.0039	-0.2014 ± 0.0039	-0.2021 ± 0.0039
$10^3 b_{\eta, \text{CIV}}(\text{eff})$	-5.4 ± 2.7	-5.2 ± 2.6	-5.2 ± 2.6	-5.2 ± 2.6
$10^3 b_{\eta, \text{SiII}}(119)$	-3.0 ± 0.5	-2.9 ± 0.5	-2.8 ± 0.5	-2.8 ± 0.5
$10^3 b_{\eta, \text{SiII}}(119.3)$	-1.7 ± 0.5	-1.7 ± 0.5	-1.7 ± 0.5	-1.7 ± 0.5
$10^3 b_{\eta, \text{SiII}}(126)$	-2.1 ± 0.6	-2.1 ± 0.6	-2.1 ± 0.6	-2.1 ± 0.6
$10^3 b_{\eta, \text{SiII}}(120.7)$	-4.4 ± 0.5	-4.8 ± 0.5	-5.0 ± 0.5	-5.2 ± 0.5
b_{HCD}	-0.0518 ± 0.0045	-0.0476 ± 0.0045	-0.0467 ± 0.0045	-0.0468 ± 0.0045
β_{HCD}	0.6051 ± 0.0831	0.5985 ± 0.0839	0.5976 ± 0.0840	0.6003 ± 0.0840
$10^2 A_{\text{sky, auto}}$	0.95 ± 0.6	0.94 ± 0.6	0.94 ± 0.6	0.94 ± 0.6
$\sigma_{\text{sky, auto}}$	31.42 ± 1.68	31.78 ± 1.69	31.89 ± 1.69	31.93 ± 1.69
Ly α \times quasar cross-correlation				
Prob.	0.200	0.184	0.175	0.169
χ^2_{\min}	3236.92	3241.58	3244.22	3246.17
α_{\parallel}	1.0617 ± 0.0321	1.0544 ± 0.0341	1.0509 ± 0.0349	1.0486 ± 0.0354
α_{\perp}	0.9289 ± 0.0381	0.9300 ± 0.0415	0.9331 ± 0.0431	0.9365 ± 0.0446
$\beta_{\text{Ly}\alpha}$	1.9311 ± 0.1428	2.1266 ± 0.1649	2.2282 ± 0.1761	2.3135 ± 0.1851
$b_{\text{Ly}\alpha}$	-0.1127 ± 0.0052	-0.1033 ± 0.0048	-0.0995 ± 0.0047	-0.0969 ± 0.0045
$b_{\eta, \text{Ly}\alpha}$	-0.2242 ± 0.0103	-0.2265 ± 0.0105	-0.2285 ± 0.0107	-0.2311 ± 0.0108
$10^3 b_{\eta, \text{CIV}}(\text{eff})$	-4.8	-4.8	-4.8	-4.8
$10^3 b_{\eta, \text{SiII}}(119)$	-4.7 ± 1.2	-4.6 ± 1.2	-4.6 ± 1.2	-4.6 ± 1.2
$10^3 b_{\eta, \text{SiII}}(119.3)$	2.2 ± 1.1	2.2 ± 1.2	2.2 ± 1.2	2.2 ± 1.2
$10^3 b_{\eta, \text{SiII}}(126)$	-1.9 ± 0.8	-1.8 ± 0.8	-1.8 ± 0.8	-1.8 ± 0.8
$10^3 b_{\eta, \text{SiII}}(120.7)$	-1.0 ± 1.0	-1.0 ± 1.0	-1.0 ± 1.0	-1.0 ± 1.0
b_{HCD}	-0.0501	-0.0501	-0.0501	-0.0501
β_{HCD}	0.7031	0.7031	0.7031	0.7031
β_{QSO}	0.2602	0.2602	0.2602	0.2602
ξ_0^{TP}	0.7386	0.7386	0.7386	0.7386
$\Delta r_{\parallel, \text{QSO}}(h^{-1} \text{Mpc})$	0.2261 ± 0.1256	0.2244 ± 0.1258	0.2234 ± 0.1259	0.2220 ± 0.1260
σ_{ν}	7.6993 ± 0.4453	7.9460 ± 0.4779	8.1010 ± 0.4942	8.2629 ± 0.5076
All combined				
Prob.	0.184	0.195	0.188	0.176
χ^2_{\min}	9644.85	9639.20	9643.20	9649.33
α_{\parallel}	1.0454 ± 0.0218	1.0329 ± 0.0233	1.0267 ± 0.0239	1.0225 ± 0.0245
α_{\perp}	0.9558 ± 0.0281	0.9568 ± 0.0317	0.9621 ± 0.0326	0.9674 ± 0.0335
$\beta_{\text{Ly}\alpha}$	1.6641 ± 0.0707	1.7730 ± 0.0782	1.8312 ± 0.0826	1.8847 ± 0.0866
$b_{\text{Ly}\alpha}$	-0.1172 ± 0.0019	-0.1108 ± 0.0018	-0.1077 ± 0.0017	-0.1050 ± 0.0017
$b_{\eta, \text{Ly}\alpha}$	-0.2010 ± 0.0032	-0.2024 ± 0.0032	-0.2032 ± 0.0032	-0.2039 ± 0.0032
$10^3 b_{\eta, \text{CIV}}(\text{eff})$	-5.2 ± 2.6	-4.9 ± 2.6	-4.8 ± 2.6	-4.8 ± 2.6
$10^3 b_{\eta, \text{SiII}}(119)$	-2.7 ± 0.4	-2.6 ± 0.4	-2.5 ± 0.4	-2.5 ± 0.4
$10^3 b_{\eta, \text{SiII}}(119.3)$	-1.0 ± 0.4	-1.0 ± 0.4	-1.0 ± 0.4	-1.0 ± 0.4
$10^3 b_{\eta, \text{SiII}}(126)$	-2.2 ± 0.4	-2.2 ± 0.4	-2.2 ± 0.4	-2.2 ± 0.4
$10^3 b_{\eta, \text{SiII}}(120.7)$	-3.6 ± 0.4	-4.0 ± 0.4	-4.2 ± 0.4	-4.3 ± 0.4
b_{HCD}	-0.0501 ± 0.0036	-0.0468 ± 0.0036	-0.0462 ± 0.0036	-0.0466 ± 0.0036
β_{HCD}	0.7058 ± 0.0797	0.6959 ± 0.0806	0.6957 ± 0.0807	0.7002 ± 0.0806
β_{QSO}	0.2593 ± 0.0058	0.2610 ± 0.0059	0.2615 ± 0.0059	0.2615 ± 0.0059
$10^2 A_{\text{sky, auto}}$	0.93 ± 0.06	0.93 ± 0.06	0.92 ± 0.06	0.92 ± 0.06
$10^2 A_{\text{sky, autoLyb}}$	1.32 ± 0.09	1.31 ± 0.09	1.31 ± 0.09	1.31 ± 0.09
$\sigma_{\text{sky, auto}}$	31.42 ± 1.69	31.84 ± 1.70	31.94 ± 1.70	31.99 ± 1.70
$\sigma_{\text{sky, autoLyb}}$	34.23 ± 2.31	34.54 ± 2.32	34.61 ± 2.32	34.63 ± 2.32
ξ_0^{TP}	0.7590 ± 0.0925	0.7323 ± 0.0916	0.7255 ± 0.0913	0.7252 ± 0.0912
$\Delta r_{\parallel, \text{QSO}}(h^{-1} \text{Mpc})$	0.1081 ± 0.1087	0.0868 ± 0.1088	0.0767 ± 0.1089	0.0683 ± 0.1089
σ_{ν}	6.8148 ± 0.2676	7.0160 ± 0.2817	7.0953 ± 0.2876	7.1508 ± 0.2916

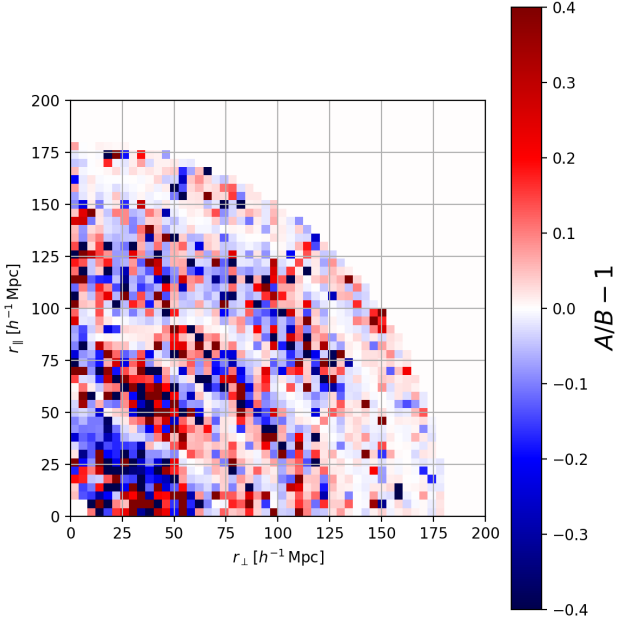


Figure 4. Comparison of Figure 3a and Figure 3b. For each pixel in Figure 3a (with reionization, labeled A) and Figure 3b (fiducial, labeled B), this plot displays the ratio A/B . To improve readability, we subtract 1 from the ratios, centering the values around zero. Around the typical BAO scale of $100 h^{-1}\text{Mpc}$, an arc of lighter pixels is evident, indicating that the impact of reionization at the BAO peak is negligible.

forest, specifically by adding the second terms in Eqs. (8) and (12) to the modeling. The impact of reionization depends inherently on its timing; however, for clarity, we first focus on incorporating a reionization model to evaluate its impact relative to the no-reionization fiducial scenario. We defer the detailed analysis of differences arising from distinct reionization histories to subsequent paragraphs. In Figure 1, we add reionization relics to the fiducial model (depicted by the purple dashed curve) while isolating the models from metal contamination to emphasize the effect of reionization. Figure 1 uses a model with late reionization – the PySR late model described by Eq. (14) – because it provides the largest differences from the no-reionization scenario. To further enhance the visual contrast with the fiducial model, some parameters have been manually adjusted, and thus, the purple dashed curve does not correspond to the best performing PySR late model. Even though reionization relics generally introduce additional broadband power to the Ly α forest correlation function, the curve with reionization effects is not guaranteed to always be above the fiducial model. The power boost for this μ -wedge is most easily appreciable at smaller separations ($25 \lesssim r \lesssim 80 h^{-1}\text{Mpc}$).

It is worth noting that reionization relics contribute to the Ly α forest correlation function in a distinct way compared to other effects introduced in §3. The contribution of metal lines is primarily constrained by the peaks they generate near $r_{\perp} = 0$, while DLAs also influence the power spectrum along the LOS. Although quasars are likely to emit light anisotropically (Font-Ribera et al. 2013), the conventional method described in §3.2 assumes quasar isotropic emission and thus only depends on r with a strong decay for increasing r . In contrast, inhomogeneous reionization affects the power spectrum in both k_{\parallel} and k_{\perp} . In addition, while DLAs are localized features in the transmitted flux, the effect of patchy reionization extends across the transmitted flux – as showcased in Figure 7 of Puchwein et al. (2023). Therefore, its effects cannot be identified individually at the

spectral level. Furthermore, as mentioned in §3.3, nonlinear growth and gas pressure suppression are isotropic effects, whereas reionization relics are an anisotropic effect, with the strongest imprint appearing at small wavenumbers due to the characteristic scale of ionized bubbles. Although the suppression due to peculiar velocities – second term in Eq. (5) – is also anisotropic, it has a different behavior in both k and μ .

Furthermore, Figure 2 includes wedge plots for the full range of μ , including metal contamination. The metals primarily contribute additional bumps in the correlation function along the LOS, as evident from the features at $r \sim 20, 60, \text{ and } 111 h^{-1}\text{Mpc}$ in the top-left panel. Notably, the bottom-right panel of Figure 2 differs from Figure 1. This discrepancy is due to using a different reionization model in the former (PySR early, which happens to provide the best fit to the data) and because Figure 1 does not depict a best-fit model. Besides, in Figure 1, the metal contributions are turned off prior to fitting. In general, the curve incorporating reionization in Figure 2 agrees well with the data points but shows some discrepancies with the fiducial model. While the reionization term introduces added power to the correlation function, the red curve (reionization) can appear higher or lower than the black curve (fiducial model) depending on the fit since the fitting process optimizes alignment with data points, balancing the inclusion of reionization relics. Moreover, as implied by Eq. (8), the ratio of the reionization term to the conventional Ly α term decreases with increasing μ , thus diminishing the impact of reionization. As a result, the level of discrepancy between the two models varies across different wedges. For wedges with $\mu \approx 1$, the red dashed curve tends to align more closely with the black fiducial curve, particularly at small separations below the BAO scale, where the data also have small error bars.

The BAO parameters α_{\parallel} and α_{\perp} have only minor deviations when incorporating the effects of reionization. This limited impact is expected, as the reionization term introduces relatively small perturbations to the correlation function near the BAO peak, as illustrated in Figure 1 (see also Figure 4 of Montero-Camacho et al. 2023). To visualize these subtle changes, we examine the residuals of the 3D Ly α forest auto-correlation function. The scenario incorporating reionization relics – described by the PySR early model – is shown in Figure 3a, while the fiducial model is depicted in Figure 3b. Given the difficulty of discerning the difference by eye, we plot their ratio in Figure 4. Near the typical BAO scale of $100 h^{-1}\text{Mpc}$, there is an arc of lighter pixels, indicating minimal impact of reionization relics on the BAO peak location. Additional arcs, such as the one observed around $75 h^{-1}\text{Mpc}$, correspond to transition points between the reionization model giving a larger or smaller ξ compared to the no-reionization model, which explains why there is a preference for blue points at $25 < r < 50 h^{-1}\text{Mpc}$ (for example, see the bottom-right panel of Figure 2). Note that some of these transitions are coincidentally located near the recovery from metal bumps, such as after the bump at $r = 60 h^{-1}\text{Mpc}$. Even though the location of these features are consistent across models, their amplitudes can vary due to the broadband effects of reionization. Furthermore, the Fourier transform of a Yukawa-like function yields a Lorentzian-type curve, which contributes to the stronger discrepancies – in absolute value – between models at smaller separations, as illustrated in Figure 4.

To quantify the influence of reionization in this analysis, we tabulate the best-fit parameter values in Table 1. From top to bottom, the table lists results for Ly α (Ly α) \times Ly α (Ly α), Ly α (Ly α) \times quasar, and the combined correlation – including Ly α (Ly α) \times Ly α (Ly β), Ly α (Ly β) \times quasar, and the two aforementioned correlation functions. Consistent with expectations, the BAO parameters exhibit only minor deviations upon including reionization relics. For instance,

for the PySR early model, α_{\parallel} deviates by 1.9% and α_{\perp} by 1.0%. In contrast, other cosmological parameters show more significant shifts. The Ly α forest bias factor ($b_{\text{Ly}\alpha}$) shifts by 4.7%, surpassing the 1σ range of the fiducial model. Likewise, the corresponding RSD parameter ($\beta_{\text{Ly}\alpha}$) shifts by 5.4%. Metal line biases remain largely unchanged, which is expected because the reionization relics produce a broadband effect and is only included in the modeling of the Ly α term. Other nuisance parameters, like A_{sky} and σ_{sky} , also remain essentially unchanged.

The results for the cross-correlation mirror those of the auto-correlation for the BAO parameters, even after incorporating the reionization term. However, significant variations are present, particularly in the Ly α bias and RSD parameter, while other non-BAO parameters remain largely unaffected. A notable difference from the auto-correlation function is the larger deviation from unity between α_{\parallel} and α_{\perp} in the cross-correlation dataset, a trend consistent with what was observed for the fiducial model. Furthermore, $\beta_{\text{Ly}\alpha}$ has a considerably larger value in the cross-correlation analysis than in the auto-correlation – $\beta_{\text{Ly}\alpha}^{\text{cross}} = 1.9311 \pm 0.1428$ versus $\beta_{\text{Ly}\alpha}^{\text{auto}} = 1.6331 \pm 0.0864$. This divergence is further reinforced by the inclusion of reionization relics. These discrepancies between the two datasets likely arise from the lower constraining power of the cross-correlation and also due to the implicit subspace of parameter space that is selected by fixing some of the model parameters.

We now change our focus to the influence of different reionization timelines, represented in our work by the early, mid, and late scenarios. These scenarios consistently yield α_{\parallel} and α_{\perp} values within 1σ agreement with the fiducial model across all correlations, as shown in Figure 5. An interesting trend is the apparent convergence of α_{\parallel} and α_{\perp} toward unity with progressively later reionization models, although this trend appears to lack statistical or physical significance to our best knowledge. As mentioned above, the strongest effects of reionization are observed in $b_{\text{Ly}\alpha}$ and $\beta_{\text{Ly}\alpha}$ with a shift in the PySR early scenario of 5.4% for the RSD parameter. The deviation increases with later reionization scenarios, as shown in Figure 6. From the fiducial to the PySR early, mid, and late models, the influence of reionization grows progressively, leading to an increase in both $\beta_{\text{Ly}\alpha}$ and $b_{\text{Ly}\alpha}$. Notably, in the PySR late model, $\beta_{\text{Ly}\alpha}$ exceeds the 3σ range of the fiducial model, while $b_{\text{Ly}\alpha}$ can reach shifts greater than 6σ . These results underscore the substantial impact of reionization relics on the Ly α forest.

We hypothesize that the observed effect on the biases is due to the minimizer attempting to balance the additional power introduced by reionization relics. According to Eq. (8), the Ly α contribution is modulated by $\beta_{\text{Ly}\alpha}$ to the second power via the Kaiser term, while the reionization term depends on $\beta_{\text{Ly}\alpha}$ to the first power instead. Consequently, as $\beta_{\text{Ly}\alpha}$ increases, the relative contribution of the reionization perturbation diminishes. In scenarios with later reionization, the amplitude of the reionization term increases, prompting a corresponding increase in $\beta_{\text{Ly}\alpha}$ to suppress the relative influence of the reionization term. An analog trend is evident for $b_{\text{Ly}\alpha}$ in Eq. (8), which explains why its value decreases (in absolute value) with the increasing impact of reionization relics, as can be seen in Figure 7.

We note that our covariance matrices are underestimated due to the exclusion of cross-covariance terms among the different correlation functions in the eBOSS DR16 analysis, which has been shown to result in a 10% underestimation of uncertainties in BAO parameters (Cuceu et al. 2024). This underestimation likely extends to other parameters but it is insufficient to account for the magnitude of the observed differences in bias and RSD parameters. However, non-BAO parameters are known to be sensitive to analysis choices (see

Figure 11 and surrounding text in DESI Collaboration et al. 2024a). This variability could obscure the quantitative significance of the shifts in $b_{\text{Ly}\alpha}$ and $\beta_{\text{Ly}\alpha}$. Nonetheless, the qualitative preference for increased $b_{\text{Ly}\alpha}$ and $\beta_{\text{Ly}\alpha}$ in delayed reionization scenarios is likely robust and independent of analysis choices for the eBOSS DR16 catalog.

Although it uses a different quasar catalog with an increased number of tracers, the DESI Year 1 Ly α BAO analysis has not yet achieved a signal-to-noise ratio comparable to eBOSS DR16. Nevertheless, its increased density of tracers provides valuable insights into the range of non-BAO parameters. Specifically, DESI also exhibits a preference for larger Ly α bias and RSD parameters ($b_{\text{Ly}\alpha}^{\text{DESI}} = -0.1078^{+0.0045}_{-0.0054}$ and $\beta_{\text{Ly}\alpha}^{\text{DESI}} = 1.743^{+0.074}_{-0.100}$) than the eBOSS DR16.

While we observe significant deviations in the Ly α bias and RSD parameters across different reionization models, the quasar RSD parameter ($\beta_{\text{q}} \sim 0.26$) remains highly consistent in the combined analysis. However, the systematic trend of a greater RSD impact on the Ly α forest compared to that on quasars persists across all models, in agreement with DESI and eBOSS findings.

Consistent with the findings from the eBOSS DR16 analysis, the reionization models also yield Δr_{\parallel} values consistent with zero within the statistical uncertainties for the combined analysis. Hence, quasar redshifts remain unbiased. In addition, the reionization models recover values of σ_{v} that align with the estimate of the fiducial model ($\sigma_{\text{v}} = 6.8148 \pm 0.2676$), and thus indicate that the Lorentzian profile, utilized in the nonlinear quasar modeling to capture the impact of random peculiar velocities and redshift errors (see §3.3), remains effective.

Our analysis incorporates four distinct models and multiple correlation functions, each with varying degrees of constraining power and thus different preferences for the model that best fits the data. The Ly α auto-correlation has a clear preference for the PySR early model, as indicated by its highest p -value and lowest minimum χ^2 , as tabulated in Table 1. While this preference decreases progressively as the reionization timeline shifts from early to late, models with reionization relics consistently outperform the fiducial model. However, this trend does not hold for the Ly α \times quasar cross-correlation, where the fiducial model provides a better fit compared to models that include reionization relics. This outcome can be partly attributed to the relatively lower quality of the data used in the cross-correlation analysis. Another contributing factor is that some of the model parameters are fixed, such as the quasar RSD parameter, the carbon bias, and the quasar proximity parameter. These fixed parameters restrict the fit to a constrained subspace of the parameter manifold, potentially biasing the computation against the inclusion of reionization relics. The fixed values, selected from du Mas des Bourboux et al. (2020), inherently exclude the impact of reionization and may slightly overestimate the fiducial cross-correlation value. To reinforce this last point, we multiply the fiducial cross-power spectrum by 0.9 and obtain a “better” fit, yielding a higher p -value and a lower minimum χ^2 . We interpret this as further evidence that the selected parameter space may overestimate the cross-correlation.

When combining all correlations and allowing all model parameters to vary freely, a slight preference for some reionization over the fiducial models re-emerges. Our best performing model corresponds to the PySR early model achieving a p -value of 0.195 and $\chi^2_{\text{min}} = 9639.20$, compared to 0.184 and 9644.85, respectively, for the fiducial model. Once again, we caution against directly comparing the p -values and χ^2_{min} values across different correlation functions to characterize the performance of the models. Such comparisons are

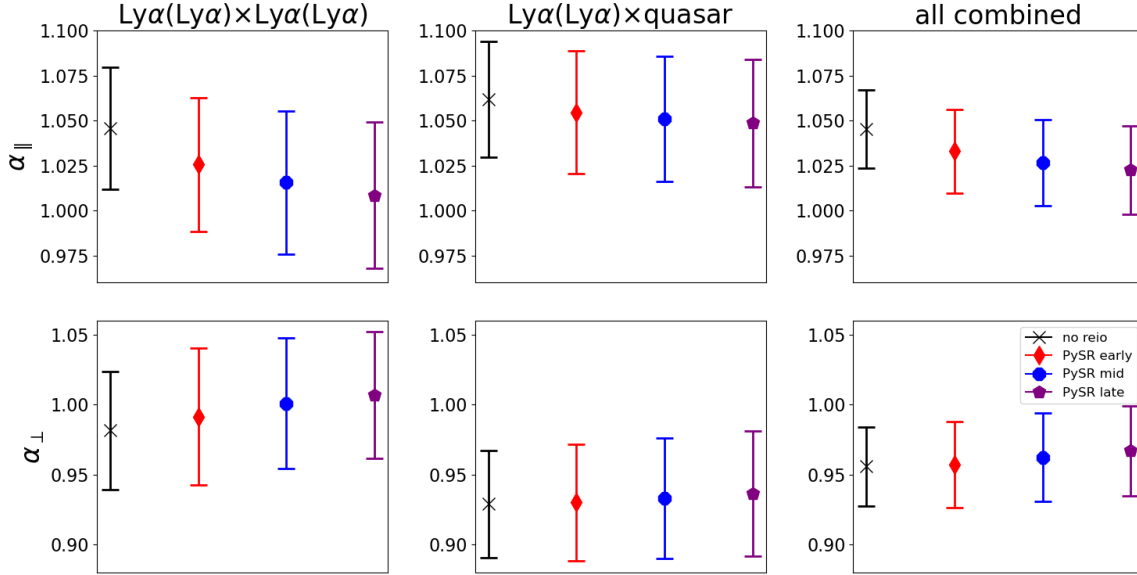


Figure 5. Comparison of constraints on the BAO parameters α_{\parallel} and α_{\perp} derived from the fiducial model (no impact of reionization) and various reionization scenarios modeled using the PySR template. Results are presented for the auto-correlation (left column), cross-correlation (center column), and the combined analysis (right column). The top row displays the inferred values of α_{\parallel} , while the bottom row corresponds to α_{\perp} . Error bars indicate the 1σ confidence, as detailed in Table 1. Across all reionization timelines, the inferred values remain consistent with those obtained from the no-reionization model.

problematic due to different number of free parameters and disparities in the quality of the data.

To contextualize the significance of the tantalizing evidence for reionization relics observed in the eBOSS DR16 correlations, it is important to recognize that other components of the model can yield comparable improvements in fit quality. For instance, in Table 5 of Bautista et al. (2017), the inclusion of fluctuations in the ionizing UV flux (Gontcho A Gontcho et al. 2014; Pontzen 2014; Long & Hirata 2023) resulted in a decrease in the minimum chi-squared value by $\Delta\chi_{\min}^2 = -4.9$ and an associated increase in probability of 0.027 when compared to a model that ignores UV clustering in the Ly α auto-correlation¹¹. For reference, our best-performing reionization model for the Ly α auto-correlation achieves a $\Delta\chi_{\min}^2 = -7.08$, which corresponds to “strong evidence” according to the standard usage (Kass & Raftery 1995)¹², and a probability increase of 0.043 relative to the fiducial model. While a direct comparison between UV clustering and reionization models is not strictly fair due to differences in the data and the degrees of freedom, it is worth emphasizing that, as presented in Appendix C, we explore a Yukawa template with a single free parameter – matching the change in degrees of freedom associated with the UV clustering model in Bautista et al. (2017). This alternative template resulted in a similar statistical improvement, with $\Delta\chi_{\min}^2 = -9$, also corresponding to strong evidence

¹¹ Note that the DESI Year 1 Ly α BAO analysis did not find a preference for the inclusion of UV fluctuations (DESI Collaboration et al. 2024a).

¹² For the Akaike information criterion (AIC, Akaike 1974), defined as $AIC = \chi_{\min}^2 + 2n$, where n the number of fitting parameters, strong evidence for the model with the smallest AIC is achieved when $6 \leq \Delta AIC < 10$. In contrast, a range of $2 \leq \Delta AIC < 6$ indicates “positive evidence” for our best performing reionization model.

in the Jeffrey’s scale, and an accompanying probability increase of 0.049, alongside a preference for early reionization.

As shown in Table 1 and discussed above, our reionization models provide constraints on the BAO parameters ($\alpha_{\parallel}, \alpha_{\perp}$) comparable to those obtained with the fiducial model. To extract the BAO parameters, we adopt a peak-smooth decomposition – see Eq. (4) – which expresses the correlation function as

$$\xi(r_{\parallel}, r_{\perp}, \alpha_{\parallel}, \alpha_{\perp}) = \xi_{\text{sm}}(r_{\parallel}, r_{\perp}) + \xi_{\text{peak}}(\alpha_{\parallel} r_{\parallel}, \alpha_{\perp} r_{\perp}). \quad (21)$$

The BAO parameters are defined as

$$\alpha_{\parallel} = \frac{[D_H(z_{\text{eff}})/r_d]}{[D_H(z_{\text{eff}})/r_d]_{\text{fid}}} \quad \text{and} \quad \alpha_{\perp} = \frac{[D_M(z_{\text{eff}})/r_d]}{[D_M(z_{\text{eff}})/r_d]_{\text{fid}}}, \quad (22)$$

where $D_M(z) = (1+z)D_A(z)$ is the comoving angular diameter distance, $D_H(z) = c/H(z)$ is the Hubble distance, and r_d is the sound horizon. The fiducial values for these ratios are calculated within the Λ CDM cosmology of Planck Collaboration et al. (2016):

$$\begin{cases} [D_H(z = 2.334)/r_d]_{\text{fid}} &= 8.6011 \\ [D_M(z = 2.334)/r_d]_{\text{fid}} &= 39.2035 \end{cases} \quad (23)$$

Substituting the fiducial values, the constraints on α_{\parallel} and α_{\perp} can be converted into constraints on the corresponding distance ratios. When combining all four correlation functions and using the fiducial model, the resulting distances are

$$\begin{cases} D_H(z = 2.334)/r_d &= 8.99^{+0.19}_{-0.19} \\ D_M(z = 2.334)/r_d &= 37.5^{+1.1}_{-1.1} \end{cases} \quad (24)$$

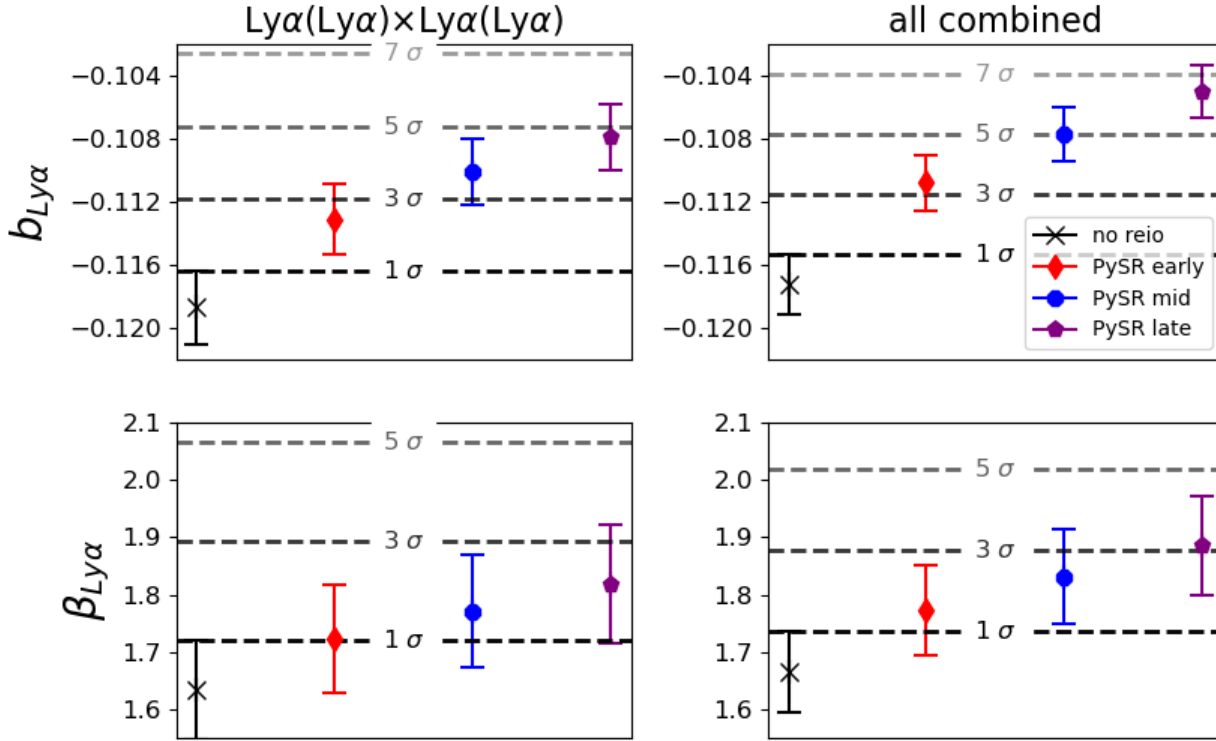


Figure 6. Similar to Figure 5 but focusing on the $\text{Ly}\alpha$ bias and redshift space distortion parameter. The left and right columns correspond to the auto-correlation and the full correlation combination, respectively. The upper (lower) row presents the constraints on $b_{\text{Ly}\alpha}$ ($\beta_{\text{Ly}\alpha}$). The dashed lines describe different confidence levels based on the 1σ errors of the fiducial model.

Similarly, for the PySR early reionization model, we obtain

$$\begin{cases} D_H(z = 2.334)/r_d = 8.88^{+0.20}_{-0.20} \\ D_M(z = 2.334)/r_d = 37.5^{+1.2}_{-1.2} \end{cases} \quad (25)$$

Since the BAO parameters have slightly non-gaussian uncertainties, it is not straightforward to define appropriate confidence intervals. While [du Mas des Bourboux et al. \(2020\)](#) used fastMC to generate 1000 realizations and map (68.27%, 95.45%) confidence levels to $\Delta\chi^2$ values, we opt for a different approach due to limited computational resources and environmental impact. Specifically, we use `MINUIT` to estimate the 1σ errors for the BAO parameters. When calculating the 1σ errors, the fitting algorithm strikes a balance between minimizing the residuals of the sum of squared differences and approximating a Gaussian fit. Note that this methodology has an over-reliance on the Gaussianity of the data for higher confidence levels.

The eBOSS DR16 data is better fitted by a model incorporating reionization relics, with an earlier reionization timeline featuring a midpoint at $z = 8.08$. This value of midpoint is higher than the midpoint inferred indirectly from CMB data ($z \approx 7.7$) but remains within the 1σ uncertainty reported by [Planck Collaboration et al. \(2020\)](#). Our results align with recent findings driven by data from the James Webb Space Telescope (JWST; [Gardner et al. 2006](#)). JWST’s capabilities enable unprecedented observations of high-redshift quasars (e.g., [Eilers et al. 2023](#)) and high-redshift galaxies (e.g., [Adams](#)

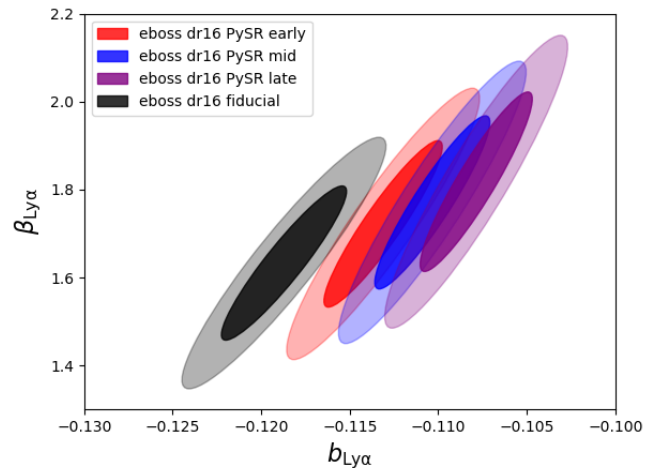


Figure 7. Contour plot of $\beta_{\text{Ly}\alpha}$ and $b_{\text{Ly}\alpha}$ for the fiducial and the PySR reionization models. The plot highlights a preference for larger RSD parameters and smaller (in absolute value) biases in later reionization scenarios. As indicated in Eq. (8), a smaller bias suppresses the overall $\text{Ly}\alpha$ power while a larger RSD counteracts this suppression to some extent while simultaneously reducing the relative importance of the reionization term compared to the baseline $\text{Ly}\alpha$ power spectrum.

et al. 2023). JWST data suggests that structure formation may have progressed slightly faster than predicted by the concordance model (Muñoz et al. 2024), which could be interpreted as evidence for earlier reionization. In contrast, late reionization is favored by measurements of the Ly α effective optical depth (Bosman et al. 2022), CMB data using an universal shape for the timeline of reionization that captures the dependence of reionization with cosmology instead of a symmetric hyperbolic tangent (Montero-Camacho et al. 2024a), and potentially measurements of the Ly α mean free path (Gao et al. 2024). While our primary analysis was restricted to reionization models described in Montero-Camacho et al. (2023) – namely, the early and late reionization scenarios that span a range around Planck’s 1σ uncertainty – Appendix C introduces a Yukawa model with a free amplitude, allowing the exploration of even earlier reionization scenarios. Remarkably, the best fit using the combination of all correlation functions correspond to a reionization amplitude of $A_{\text{re}} = 0.1900 \pm 0.0702$, which is remarkably close to the value associated with the Yukawa early reionization model ($A_{\text{re}} = 0.2088$).

5 DISCUSSION

Our results indicate that eBOSS data overall favors models that incorporate the impact of reionization in the post-reionization IGM over conventional models that neglect this effect. Nonetheless, there remain some interesting avenues to consider regarding the modeling of reionization relics and their effects, particularly at higher redshifts $z \geq 3$.

The high-redshift Ly α forest window into the IGM is increasingly recognized as a critical probe of cosmological structure formation. Alongside this growing importance is the necessity for better tools to derive accurate statistical insights from Ly α forest spectra. For instance, Sun et al. (2023) recently introduced Quasar Factor Analysis (QFA), a new continuum fitting method based on unsupervised learning and latent factor analysis. This novel methodology achieves remarkable accuracy, with errors of less than one percent in the Ly α forest one-dimensional power spectrum at $z = 3$. Such advancements are promising for studies leveraging the high-redshift Ly α window, particularly for analyses accounting for reionization relics in the Ly α forest or its cross-correlations (Montero-Camacho et al. 2025). Moreover, the high-redshift Ly α window provides a valuable opportunity to investigate small-scale effects before nonlinearities become dominant, offering an ideal environment to constrain dark matter candidates (see e.g. Puchwein et al. 2023; Zhao et al. 2024). Given these ambitious cosmological programs at high redshift, an open question arises: how might improved continuum-fitting methods, specifically optimized for high-redshifts Ly α skewers, influence the results presented in Table 1? We leave this exploration to future work.

Likewise, alternative continuum-fitting methodologies (e.g. Turner et al. 2024; Sun et al. 2023; Greig et al. 2024) are also relevant due to their impact on the standard Ly α forest analysis. The standard continuum-fitting procedure, which assumes a universal template for the quasar continuum $\bar{C}(\lambda_{\text{rf}})$ (e.g., Ramírez-Pérez et al. 2024), often modulated by a low-order polynomial, can sometimes yield unphysical results such as negative continuum estimates for specific spectra. For example, DESI Collaboration et al. (2024a) reported that 3.6% and 4.4% of the forests in the Ly α and Ly β regions, respectively, were discarded due to negative continuum.

Furthermore, in this work, we focused on the impact of inhomogeneous H I reionization. While hydrogen constitutes the majority of the baryonic content of the Universe, a significant fraction is

helium. The first reionization of helium occurs concurrently with hydrogen reionization; however, the reionization of He II takes place later, around $z \sim 3$ (Gaikwad et al. 2021), introducing further disruptions to the thermal state of the IGM that subsequently affect the Ly α forest (Greig et al. 2015). Consequently, we emphasize that the impact of He II reionization on Ly α forest correlations is likely to alter the best-fit parameters and must also be investigated. Recent studies (e.g., Bird et al. 2023; Fernandez et al. 2024) have dedicated efforts along these lines but lack the mass resolution necessary to fully resolve the high-entropy mean-density (HEMD) phase of the IGM evolution (Hirata 2018), which is crucial for modeling the long-lasting relics of H I reionization (Montero-Camacho et al. 2019; Montero-Camacho & Mao 2020). Achieving high mass resolution is essential for accurately tracking the response of gas to the passage of an ionization front, as the Jeans length increases with temperature.

Regardless of the effects of He II reionization in the IGM, our findings conclusively indicate that the eBOSS DR16 Ly α correlations prefer an additional source of power. Whether this trend is entirely due to the HEMD phase of the temperature-density relation – responsible for the long-lasting relics from H I reionization – or involves a combination of He II reionization relics mixed-in, remains an open question to be explored in future work.

Although eBOSS data appears to favor the inclusion of reionization effects, this preference has only a minor impact on cosmology derived from BAO analyses, as evidenced by the small shifts on α_{\parallel} and α_{\perp} (see Figure 5). In contrast, the significant influence on bias and redshift-space distortion parameters underscores the strong effect on full-shape analyses of the Ly α forest (Font-Ribera et al. 2018; Cuceu et al. 2023; Gerardi et al. 2023), with the potential to introduce significant biases. Future work will explore the signatures of reionization relics in measurements of the one-dimensional Ly α forest power spectrum.

Nonlinear broadening of the BAO peak can substantially affect the estimated BAO errors (DESI Collaboration et al. 2024a), motivating the need for more sophisticated and accurate nonlinear modeling approaches. In §3.3, we discussed the standard nonlinear modeling applied in Ly α BAO analyses; however, the treatment of the quasars remains relatively simplistic compared to that of the auto-correlation. Givans et al. (2022) and Chudaykin & Ivanov (2025) introduced significant improvements to the nonlinear modeling of the cross-correlation. Despite these advancements, we chose not to adopt their formalism in this work to maintain consistency with the modeling choices employed in the eBOSS DR16 analysis.

Previous works have considered the addition of broadband polynomial corrections to the baseline analysis of the Ly α correlation functions. The primary motivation of such tests is to demonstrate that the BAO parameters remain stable even in the presence of potential systematic effects unaccounted for in the modeling. These validation tests have relevant parallels to the memory of reionization, as their imprint manifests as a broadband effect.

The broadband terms are often introduced with informative priors on certain non-BAO parameters and are coupled with restricted separation range to minimize their influence at small separations. (For example, Bautista et al. 2017 uses $40 < r < 180 h^{-1} \text{Mpc}$.) Compared to their baseline analyses, Bautista et al. (2017) and DESI Collaboration et al. (2024a) found slightly larger α_{\parallel} and smaller α_{\perp} when including broadband terms. In contrast, du Mas des Bourboux et al. (2020) reported that the inclusion of broadband terms with physical priors resulted in a slight increase in both BAO parameters relative to the baseline model. Our results with reionization relics (see Figure 5) reveal a distinct trend: the broadband effects of reion-

ization lead to a small negative shift in α_{\parallel} and a positive shift in α_{\perp} .

These seemingly contradictory results are not necessarily indicative of tension. The implementation of the broadband polynomial correction adds 12 new free parameters per correlation function to the analysis. This addition is paired with a restricted range of separations and relies on priors to break degeneracies in parameters that require information from small separations. Conversely, the model presented in this work introduces no additional free parameters¹³ and utilizes the same separation range as the fiducial analysis¹⁴. Even a qualitative comparison by eye can already discern subtle differences between our model (Figure 2) and the broadband corrections presented in Figure 18 of [du Mas des Bourboux et al. \(2020\)](#), Figure 14 in [Bautista et al. \(2017\)](#), and Figure 4 in [DESI Collaboration et al. \(2024a\)](#).

Similarly, [du Mas des Bourboux et al. \(2020\)](#) reported that shifts in the BAO parameters due to the broadband corrections – with physical priors – were accompanied by a significant decrement in $\beta_{Ly\alpha}$ and a strong reduction in the bias $b_{\eta, Ly\alpha}$ (see their Table 11). When the priors were relaxed, however, the RSD parameter was found to increase relative to the baseline value, while the bias decreased more sharply. Notably, the no-prior broadband model also produced trends in the BAO parameters similar to those observed in this work, specifically a negative shift in α_{\parallel} and a positive shift in α_{\perp} . Our findings align more closely with the no-prior results. Table 1 shows an increase in the RSD parameter, accompanied by a decrease in $b_{\eta, Ly\alpha}$ with respect to the fiducial scenario¹⁵.

6 CONCLUSIONS

The $Ly\alpha$ forest correlation functions have proven successful for probing the evolution of the Universe at redshifts that are typically inaccessible to galaxy surveys. In the era of stage IV spectroscopic surveys, DESI has already produced intriguing findings, including a potential preference for dynamic dark energy ([DESI Collaboration et al. 2024b](#)), which could have significant repercussions for cosmological constraints on the sum of the neutrino masses (e.g., [Du et al. 2024](#)). With the enhanced statistical power provided by DESI observations and the anticipated capabilities of next-generation stage V spectroscopic instruments, such as the MULTiplexed Survey Telescope (MUST; [Zhao et al. 2024](#)), addressing potential biases from known contaminants in the $Ly\alpha$ forest correlations is a critical task.

This work builds extensively upon prior efforts that have meticulously identified various contaminants, systematics, and modeling challenges in $Ly\alpha$ correlations ([du Mas des Bourboux et al. 2020](#); [Bautista et al. 2017](#); [Gordon et al. 2023](#), and references therein). Here, we have investigated the impact of an additional factor affecting $Ly\alpha$ forest correlation functions, namely the impact of inhomogeneous reionization. Reionization leaves enduring imprints that survive for billions of years, well into the post-reionization era (e.g., [Montero-Camacho et al. 2019](#)). These reionization relics induce a broadband

enhancement in power within the correlation functions ([Montero-Camacho et al. 2023](#)), and thus impacting full-shape analysis significantly.

Here, we present the first analysis of the impact of reionization on $Ly\alpha$ forest correlations using the publicly available eBOSS DR16. Our findings can be summarized as follows:

- The BAO parameters (α_{\parallel} , α_{\perp}) exhibit minimal sensitivity to the inclusion of reionization effects in the modeling, irrespective of the specific reionization model and scenario considered. The largest shifts are $\Delta\alpha_{\parallel} = -0.0373$ and $\Delta\alpha_{\perp} = 0.0255$, both arising from the PySR late model applied to the $Ly\alpha$ auto-correlation function. These shifts remain well within the 1σ confidence level of the fiducial no-reionization model (see Figure 5).

- Overall, the eBOSS DR16 $Ly\alpha$ correlation data are better fitted by models that include the impact of reionization. This result represents the first tantalizing evidence of reionization relics persisting well into the post-reionization era. However, the preference is modest; for instance, an analysis encompassing all four correlation functions for the PySR early model yields $\chi^2_{\min} = 9639.20$ with a corresponding probability of 0.195, compared to $\chi^2_{\min} = 9644.85$ and a probability of 0.184 for the fiducial model without reionization effects.

- The inclusion of reionization effects into the modeling can have drastic influence on the $Ly\alpha$ bias and RSD parameters, particularly for late reionization scenarios (see Figure 6). Notably, our PySR late reionization model leads to a positive shift in $\beta_{Ly\alpha}$ exceeding 3σ , accompanied by a positive shift in $b_{Ly\alpha} \approx 7\sigma$.

- The eBOSS DR16 data favors an early reionization scenario, characterized by a reionization midpoint at $z \approx 8.1$ and an optical depth of $\tau \approx 0.0583$ ([Montero-Camacho & Mao 2020](#)), aligning well with the 1σ range reported by [Planck Collaboration et al. \(2020\)](#).

We conclude that the shape of the $Ly\alpha$ correlations can be used to constrain reionization scenarios. Besides, these effects must also be carefully incorporated into future shape-analysis efforts that aim to extend beyond BAO information (e.g. [Font-Ribera et al. 2018](#); [Cuceu et al. 2023](#); [Gerardi et al. 2023](#)). Furthermore, we underscore the vital need for high-mass resolution in simulations to accurately capture the HEMD phase of the temperature-density evolution ([Hirata 2018](#)). Simply put, simulations that fail to resolve small-scale structures prior to the onset of reionization, i.e. before the significant increase in the Jeans mass caused by ionization fronts, will inherently underestimate the long-term survival of reionization relics.

Likewise, independent of potential modeling improvements or limitations, our results clearly demonstrate that the eBOSS DR16 $Ly\alpha$ forest correlation functions have a preference for an additional source of power.

Finally, we highlight that the correlation function BAO analysis remains largely shielded from the impact of reionization. This robustness arises from two key factors: the BAO scale is significantly larger than the typical scale of reionization bubbles, and the analysis is conducted at an effective redshift of $z_{re} = 2.334$. At higher redshifts, the impact of reionization relics becomes stronger, as there is insufficient time for the IGM to relax into the usual temperature-density relation ([Hui & Gnedin 1997](#)). Given our findings, the redshift range probed directly by the one-dimensional $Ly\alpha$ power spectrum, and the expected effects of reionization relics ([Montero-Camacho & Mao 2021](#)), future work will focus on conducting the first analysis of these measurements that explicitly account for the lasting impact of inhomogeneous reionization.

¹³ In Appendix C, we introduce a reionization model with one extra parameter, which recovers the trends identified in the main analysis.

¹⁴ A run of the PySR early model restricted to the range $40 < r < 180 h^{-1} \text{Mpc}$ also recovers the same trend for the BAO parameters, i.e. a negative shift in α_{\parallel} and a positive in α_{\perp} .

¹⁵ An analysis of the PySR early model restricted to $40 < r < 180 h^{-1} \text{Mpc}$ obtains a negative shift in the RSD parameter instead, in agreement with the physical prior broadband test used in [du Mas des Bourboux et al. \(2020\)](#), while still exhibiting a different trend for the BAO parameters.

ACKNOWLEDGEMENTS

We are sincerely grateful to Abby Bault, Andreu Font-Ribera, and other members of the DESI collaboration who contributed to the tutorial for reproducing the eBOSS DR16 analysis outside of NERSC. We are also thankful to James Rich for his valuable insights. This work is supported by the National SKA Program of China (grant No. 2020SKA0110401) and the Major Key Project of PCL. We acknowledge the Tsinghua Astrophysics High-Performance Computing platform at Tsinghua University and PCL's Cloud Brain for providing computational and data storage resources that have contributed to the research results reported within this paper. This work made extensive use of the [NASA Astrophysics DataSystem](#) and the following open-source python libraries/packages: `matplotlib` (Hunter 2007), `numpy` (Harris et al. 2020), `PySR` (Cranmer 2020), `scipy` (Virtanen et al. 2020), `iminuit`, and `picca` (du Mas des Bourboux et al. 2021).

DATA AVAILABILITY

The data underlying this article will be shared on reasonable request to the corresponding authors.

REFERENCES

- Abareshi B., et al., 2022, *AJ*, 164, 207
- Abdul Karim M. L., Armengaud E., Mention G., Chabanier S., Ravoux C., Lukic Z., 2024, *J. Cosmology Astropart. Phys.*, 2024, 088
- Adams N. J., et al., 2023, *MNRAS*, 518, 4755
- Akaike H., 1974, *IEEE Transactions on Automatic Control*, 19, 716
- Alam S., et al., 2021, *Phys. Rev. D*, 103, 083533
- Alcock C., Paczynski B., 1979, *Nature*, 281, 358
- Ángela García L., et al., 2023, *arXiv e-prints*, p. arXiv:2304.05855
- Arinyo-i-Prats A., Miralda-Escudé J., Viel M., Cen R., 2015, *J. Cosmology Astropart. Phys.*, 2015, 017
- Bault A., et al., 2024, *arXiv e-prints*, p. arXiv:2402.18009
- Bautista J. E., et al., 2017, *A&A*, 603, A12
- Bird S., et al., 2023, *J. Cosmology Astropart. Phys.*, 2023, 037
- Blomqvist M., et al., 2018, *J. Cosmology Astropart. Phys.*, 2018, 029
- Bosman S. E. I., et al., 2022, *MNRAS*, 514, 55
- Chabanier S., et al., 2019, *J. Cosmology Astropart. Phys.*, 2019, 017
- Chudaykin A., Ivanov M. M., 2025, *arXiv e-prints*, p. arXiv:2501.04770
- Compostella M., Cantalupo S., Porciani C., 2013, *MNRAS*, 435, 3169
- Cranmer M., 2020, *PySR: Fast & Parallelized Symbolic Regression in Python/Julia*, doi:10.5281/zenodo.4041459, <http://doi.org/10.5281/zenodo.4041459>
- Cranmer M., Sanchez-Gonzalez A., Battaglia P., Xu R., Cranmer K., Spergel D., Ho S., 2020, *arXiv e-prints*, p. arXiv:2006.11287
- Croft R. A. C., Weinberg D. H., Bolte M., Burles S., Hernquist L., Katz N., Kirkman D., Tytler D., 2002, *ApJ*, 581, 20
- Cuceu A., Font-Ribera A., Joachimi B., Nadathur S., 2021, *MNRAS*, 506, 5439
- Cuceu A., et al., 2022a, *arXiv e-prints*, p. arXiv:2209.12931
- Cuceu A., Font-Ribera A., Nadathur S., Joachimi B., Martini P., 2022b, *arXiv e-prints*, p. arXiv:2209.13942
- Cuceu A., Font-Ribera A., Nadathur S., Joachimi B., Martini P., 2023, *Phys. Rev. Lett.*, 130, 191003
- Cuceu A., et al., 2024, *arXiv e-prints*, p. arXiv:2404.03004
- DESI Collaboration et al., 2022, *AJ*, 164, 207
- DESI Collaboration et al., 2023a, *arXiv e-prints*, p. arXiv:2306.06307
- DESI Collaboration et al., 2023b, *arXiv e-prints*, p. arXiv:2306.06308
- DESI Collaboration et al., 2024a, *arXiv e-prints*, p. arXiv:2404.03001
- DESI Collaboration et al., 2024b, *arXiv e-prints*, p. arXiv:2404.03002
- Du G.-H., Wu P.-J., Li T.-N., Zhang X., 2024, *arXiv e-prints*, p. arXiv:2407.15640
- Eilers A.-C., et al., 2023, *ApJ*, 950, 68
- Eisenstein D. J., Seo H.-J., White M., 2007, *ApJ*, 664, 660
- Ennesser L., Martini P., Font-Ribera A., Pérez-Ràfols I., 2022, *MNRAS*, 511, 3514
- Fernandez M. A., Bird S., Ho M.-F., 2024, *J. Cosmology Astropart. Phys.*, 2024, 029
- Filbert S., et al., 2023, *arXiv e-prints*, p. arXiv:2309.03434
- Font-Ribera A., Miralda-Escudé J., 2012, *J. Cosmology Astropart. Phys.*, 2012, 028
- Font-Ribera A., et al., 2012, *J. Cosmology Astropart. Phys.*, 2012, 059
- Font-Ribera A., et al., 2013, *J. Cosmology Astropart. Phys.*, 2013, 018
- Font-Ribera A., et al., 2014, *J. Cosmology Astropart. Phys.*, 2014, 027
- Font-Ribera A., McDonald P., Slosar A., 2018, *J. Cosmology Astropart. Phys.*, 2018, 003
- Gaikwad P., Srianand R., Haehnelt M. G., Choudhury T. R., 2021, *MNRAS*, 506, 4389
- Gao A., et al., 2024, *arXiv e-prints*, p. arXiv:2411.15838
- Gardner J. P., et al., 2006, *Space Sci. Rev.*, 123, 485
- Garzilli A., Magalich A., Ruchayskiy O., Boyarsky A., 2021, *MNRAS*, 502, 2356
- Gerardi F., Cuceu A., Font-Ribera A., Joachimi B., Lemos P., 2023, *MNRAS*, 518, 2567
- Givans J. J., Hirata C. M., 2020, *Phys. Rev. D*, 102, 023515
- Givans J. J., et al., 2022, *J. Cosmology Astropart. Phys.*, 2022, 070
- Gontcho A Gontcho S., Miralda-Escudé J., Busca N. G., 2014, *MNRAS*, 442, 187
- Gordon C., et al., 2023, *J. Cosmology Astropart. Phys.*, 2023, 045
- Greig B., Bolton J. S., Wyithe J. S. B., 2015, *MNRAS*, 447, 2503
- Greig B., et al., 2024, *MNRAS*, 533, 3312
- Guo Z., Martini P., 2019, *ApJ*, 879, 72
- Guy J., et al., 2024, *arXiv e-prints*, p. arXiv:2404.03003
- Harris C. R., et al., 2020, *Nature*, 585, 357
- Hirata C. M., 2018, *MNRAS*, 474, 2173
- Ho M.-F., Bird S., Garnett R., 2021, *MNRAS*, 507, 704
- Hui L., Gnedin N. Y., 1997, *MNRAS*, 292, 27
- Hunter J. D., 2007, *Computing in Science and Engineering*, 9, 90
- Iršič V., Di Dio E., Viel M., 2016, *J. Cosmology Astropart. Phys.*, 2016, 051
- Kass R. E., Raftery A. E., 1995, *Journal of the American Statistical Association*, 90, 773
- Kirkby D., et al., 2013, *J. Cosmology Astropart. Phys.*, 2013, 024
- La Plante P., Trac H., Croft R., Cen R., 2017, *ApJ*, 841, 87
- Lee K.-G., Suzuki N., Spergel D. N., 2012, *AJ*, 143, 51
- Lepori F., Iršič V., Di Dio E., Viel M., 2020, *J. Cosmology Astropart. Phys.*, 2020, 006
- Long H., Hirata C. M., 2023, *MNRAS*, 520, 948
- Long H., Morales-Gutiérrez C., Montero-Camacho P., Hirata C. M., 2023, *MNRAS*, 525, 6036
- Lyke B. W., et al., 2020, *ApJS*, 250, 8
- McDonald P., Miralda-Escudé J., Rauch M., Sargent W. L. W., Barlow T. A., Cen R., Ostriker J. P., 2000, *ApJ*, 543, 1
- McDonald P., et al., 2006, *ApJS*, 163, 80
- McQuinn M., Upton Sanderbeck P. R., 2016, *MNRAS*, 456, 47
- Molaro M., et al., 2022, *MNRAS*, 509, 6119
- Montero-Camacho P., in prep., *Modeling the Post-Reionization Era with Symbolic Regression*, In preparation
- Montero-Camacho P., Mao Y., 2020, *MNRAS*, 499, 1640
- Montero-Camacho P., Mao Y., 2021, *MNRAS*, 508, 1262
- Montero-Camacho P., Hirata C. M., Martini P., Honscheid K., 2019, *MNRAS*, 487, 1047
- Montero-Camacho P., Liu Y., Mao Y., 2023, *MNRAS*, 520, 4853
- Montero-Camacho P., Li Y., Cranmer M., 2024a, *arXiv e-prints*, p. arXiv:2405.13680
- Montero-Camacho P., Zhang Y., Mao Y., 2024b, *MNRAS*, 529, 3666
- Montero-Camacho P., Morales-Gutiérrez C., Zhang Y., Long H., Mao Y., 2025, *MNRAS*, 536, 1645
- Morales A. M., Mason C. A., Bruton S., Gronke M., Haardt F., Scarlata C., 2021, *ApJ*, 919, 120

- Muñoz J. B., Mirocha J., Chisholm J., Furlanetto S. R., Mason C., 2024, *MNRAS*, **535**, L37
- Palanque-Delabrouille N., Yèche C., Schöneberg N., Lesgourgues J., Walther M., Chabanier S., Armengaud E., 2020, *J. Cosmology Astropart. Phys.*, **2020**, 038
- Park J., Mesinger A., Greig B., Gillet N., 2019, *MNRAS*, **484**, 933
- Park H., Lukić Z., Sexton J., Alvarez M., 2023, *arXiv e-prints*, p. [arXiv:2309.04129](https://arxiv.org/abs/2309.04129)
- Parks D., Prochaska J. X., Dong S., Cai Z., 2018, *MNRAS*, **476**, 1151
- Percival W. J., White M., 2009, *MNRAS*, **393**, 297
- Planck Collaboration et al., 2016, *A&A*, **594**, A13
- Planck Collaboration et al., 2020, *A&A*, **641**, A6
- Pontzen A., 2014, *Phys. Rev. D*, **89**, 083010
- Puchwein E., et al., 2023, *MNRAS*, **519**, 6162
- Ramírez-Pérez C., et al., 2024, *MNRAS*, **528**, 6666
- Rauch M., 1998, *ARA&A*, **36**, 267
- Ravoux C., et al., 2023, *MNRAS*, **526**, 5118
- Rogers K. K., Bird S., Peiris H. V., Pontzen A., Font-Ribera A., Leistedt B., 2018, *MNRAS*, **476**, 3716
- Rudie G. C., Steidel C. C., Shapley A. E., Pettini M., 2013, *ApJ*, **769**, 146
- Saha A. K., Singh A., Parashari P., Laha R., 2024, *arXiv e-prints*, p. [arXiv:2409.10617](https://arxiv.org/abs/2409.10617)
- Slosar A., et al., 2011, *J. Cosmology Astropart. Phys.*, **2011**, 001
- Sun Z., Ting Y.-S., Cai Z., 2023, *ApJS*, **269**, 4
- Tie S. S., Weinberg D. H., Martini P., Zhu W., Peirani S., Suarez T., Colombi S., 2019, *MNRAS*, **487**, 5346
- Turner W., et al., 2024, *arXiv e-prints*, p. [arXiv:2405.06743](https://arxiv.org/abs/2405.06743)
- Udrescu S.-M., Tegmark M., 2020, *Science Advances*, **6**, eaay2631
- Upton Sanderbeck P., Bird S., 2020, *MNRAS*, **496**, 4372
- Valluri M., et al., 2022, *arXiv e-prints*, p. [arXiv:2203.07491](https://arxiv.org/abs/2203.07491)
- Viel M., Haehnelt M. G., Springel V., 2004, *MNRAS*, **354**, 684
- Viel M., Lesgourgues J., Haehnelt M. G., Matarrese S., Riotto A., 2005, *Phys. Rev. D*, **71**, 063534
- Virtanen P., et al., 2020, *Nature Methods*, **17**, 261
- Wang B., et al., 2022, *ApJS*, **259**, 28
- Wells A., Robinson D., Avestruz C., Gnedin N. Y., 2024, *MNRAS*, **528**, 5845
- Wu X., McQuinn M., Kannan R., D’Aloisio A., Bird S., Marinacci F., Davé R., Hernquist L., 2019, *MNRAS*, **490**, 3177
- Yang L., et al., 2022, *ApJ*, **935**, 121
- Yèche C., Palanque-Delabrouille N., Baur J., du Mas des Bourboux H., 2017, *J. Cosmology Astropart. Phys.*, **2017**, 047
- Youles S., et al., 2022, *MNRAS*, **516**, 421
- Zhao C., et al., 2024, *arXiv e-prints*, p. [arXiv:2411.07970](https://arxiv.org/abs/2411.07970)
- de Belsunce R., Philcox O. H. E., Iršič V., McDonald P., Guy J., Palanque-Delabrouille N., 2024, *MNRAS*, **533**, 3756
- du Mas des Bourboux H., et al., 2019, *ApJ*, **878**, 47
- du Mas des Bourboux H., et al., 2020, *ApJ*, **901**, 153
- du Mas des Bourboux H., et al., 2021, picca: Package for Igm Cosmological Correlations Analyses, Astrophysics Source Code Library, record ascl:2106.018

APPENDIX A: YUKAWA TEMPLATE PARAMETER VALUES

Table A1 presents the Yukawa template parameters from Eq. (9) at the effective redshift of the correlation functions. The parameter A_{re} is the amplitude of the reionization relics, while α_{re}^{-1} corresponds to the effective range of the Yukawa-like interaction (Montero-Camacho et al. 2023). This screening mechanism reflects the expected behavior of reionization relics, which are coupled to the characteristic scales of reionization bubbles – \mathcal{O} (a few Mpc) – and are significantly suppressed at smaller bubbles. The coefficient β_{re} governs the large-scale shape of the template. Note that earlier reionization leads to smaller (larger) values of A_{re} and α_{re} (β_{re}).

Table A1. Template parameters for the different reionization scenarios within the Yukawa model evaluated at z_{eff} .

Reionization model	A_{re}	α_{re}	β_{re}
Yukawa early	0.2088	0.7239	2.3656
Yukawa mid	0.4775	1.5094	2.1774
Yukawa late	1.5050	3.0237	1.8354

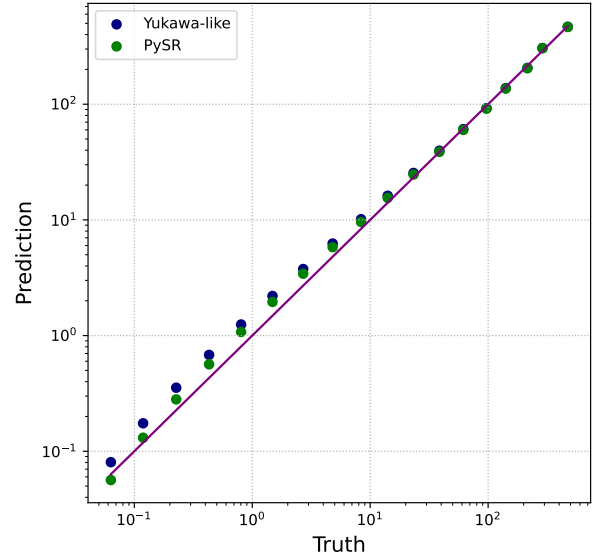


Figure B1. Performance comparison of the reionization templates: the symbolic regression-based template derived using PySR (green dots) and the Yukawa-like template from Montero-Camacho et al. 2023 (blue dots). The purple line corresponds to the diagonal where predictions perfectly match the ground truth.

APPENDIX B: REIONIZATION TEMPLATES: PYSR VS YUKAWA

Here, we evaluate the performance of our two methodologies designed to account for the impact of reionization on the post-reionization $\text{Ly}\alpha$ forest, i.e. the PySR template (Eq. 11; Montero-Camacho prep), and the Yukawa-like template (Eq. 9; Montero-Camacho et al. 2023). Our comparison begins with assessing the templates’ ability to reproduce data from simulations. We focus on high-redshift data ($z = 4$), where the imprints of reionization in the $\text{Ly}\alpha$ forest are stronger.

Figure B1 demonstrates the performance of Eq. (11) in capturing the memory of reionization within the $\text{Ly}\alpha$ forest 3D power spectrum – see Montero-Camacho (prep) for further details. The symbolic regression-based template derived using PySR outperforms the analytical Yukawa-like template in accuracy. Additionally, the PySR template achieves a marginally higher R^2 metric, with a value of 0.9982 compared to 0.9981 for the Yukawa-like template.

Considering the small degree of deviation between both templates and their similarly high predictive accuracy, we anticipate negligible bias between models utilizing either template. This is a promising outcome, as the PySR-based template achieves this performance without introducing additional degrees of freedom for fitting across different redshift bins – as long as the redshift range is covered by the training data.

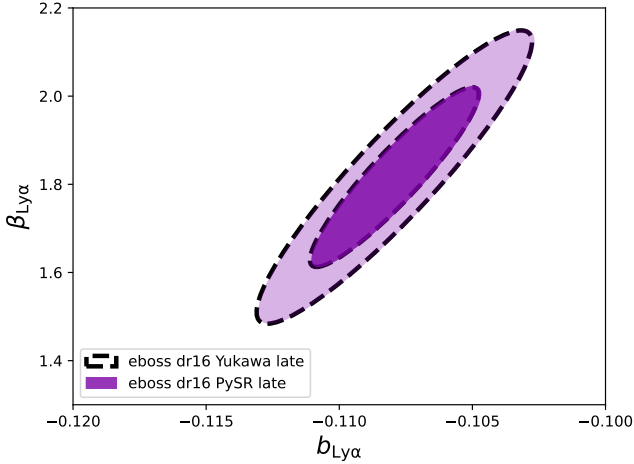


Figure B2. Contour plot of $\beta_{\text{Ly}\alpha}$ and $b_{\text{Ly}\alpha}$ for the Yukawa late model and the PySR late model. The near-complete overlap of the two contours suggests that the models yield largely equivalent results.

To facilitate comparison between the two approaches applied to real data, we tabulate the results of the Yukawa analyses of the eBOSS DR16 Ly α correlations in the last three columns of Table C1. Comparing these results with those discussed in the main body of the paper reveals excellent agreement in the shifts of the BAO parameters between the two templates. Furthermore, these shifts remain consistent with the fiducial model without reionization relics, all within 1σ . This consistency arises because the effects of reionization do not couple with the BAO scale, as illustrated in Figure 4.

To verify that the different templates yield consistent results regarding the impact of reionization on non-BAO parameters that are more sensitive to such broadband perturbations, we plot the confidence ellipses for the Ly α bias and the Ly α RSD parameter in Figure B2 for the Yukawa late and PySR late templates. Figure B2 demonstrates the remarkable agreement between the two models.

APPENDIX C: YUKAWA TEMPLATE WITH ONE FREE PARAMETER

Our main analysis leverages reionization templates to model the lasting impact of reionization on the Ly α forest. These templates are derived from a simulation suite (Montero-Camacho & Mao 2020; Montero-Camacho et al. 2023) encompassing three distinct reionization scenarios, centered on the reionization midpoint inferred from CMB data (Planck Collaboration et al. 2020). To increase the flexibility of our templates and accommodate a broader range of reionization histories, we incorporate a Yukawa-like template (see Eq. 9) in which the amplitude parameter A_{re} is allowed to vary, while the parameters α_{re} and β_{re} are fixed to their respective values for each reionization scenario (described in Table A1). Since A_{re} represents an amplitude of a power spectrum, we impose a physically motivated prior of $A_{\text{re}} \geq 0$. To distinguish these models from the Yukawa templates with fixed amplitude values, we designate them with a “(+)” notation, e.g. Yukawa early(+).

Besides enabling a broader exploration of reionization histories within the parameter space, the amplitude A_{re} is also intrinsically related to the underlying cosmology. For instance, higher values of the matter density Ω_{m} will hasten the reionization process (Montero-Camacho et al. 2024a), leading to lower values of A_{re} . Thus, if

the analysis of the data returned a best-fit result that deviates from expectations associated with earlier reionization, it may also indicate a preference for a particular region within the cosmological parameter space.

We present our results with the Yukawa template with one free parameter in Table C1. The auto-correlation is best fitted by a model with A_{re} values roughly consistent with an early reionization scenario. Interestingly, allowing the amplitude to vary produces similar values of $\beta_{\text{Ly}\alpha}$ and $b_{\text{Ly}\alpha}$ across different reionization models, while simultaneously maintaining the previously observed trends: a decrease in α_{\parallel} and a positive shift in α_{\perp} relative to the no reionization model. The consistency in bias and RSD parameters may be interpreted as another sign of a compensatory mechanism when using the other templates. Specifically, there is a decrease (in absolute value) in $b_{\text{Ly}\alpha}$ from early to late reionization scenarios, resulting in reduced power in the Ly α power spectrum. Meanwhile, $\beta_{\text{Ly}\alpha}$ appears to counteract this trend by shifting in the opposite direction to modulate the overall strength, as shown in Figure 7.

The inclusion of a free parameter in the reionization model can improve the fit of the cross-correlation, but this improvement is primarily due to effectively turning off the reionization model. Therefore, the cross-correlation between Ly α and quasars still shows a preference for the fiducial model. As discussed in §4, the cross-correlation is less constraining than the auto-correlation, and statistical fluctuations may drive this preference. More interestingly, this behavior may be indicative of imprecision in the modeling. Nonlinearities in the quasar modeling could play a significant role (Givans et al. 2022), but it is also possible that our assumption of no reionization imprints in the quasar model is incorrect. The assumption stems from the expectation for the baryonic modulation effect of reionization in shallow potential wells (Long & Hirata 2023; Montero-Camacho et al. 2025). However, quasars likely form in denser environments, which could make them more resilient to reionization effects. Another intriguing possibility is that quasars may be better described by a different cosmological model. Table 9 of du Mas des Bourboux et al. (2020) hints that the cross-correlation in eBOSS DR16 is better fit by an alternative cosmology. Nevertheless, the most plausible explanation for these trends is that they originate from the weaker constraining power.

For the combination of all correlations, the best fit gives $A_{\text{re}} \approx 0.19$, which is in good agreement with the value corresponding to our early reionization model and consistent with the 1σ range from Planck Collaboration et al. (2020). The free A_{re} templates also recover the same trends for the shifts in the BAO, bias, and RSD parameters relative to the fiducial model. Notably, both the Yukawa mid(+) and Yukawa late(+) models show a systematic preference for lower values of A_{re} , and thus signaling a preference for reionization to occur earlier across the board.

This paper has been typeset from a \LaTeX file prepared by the author.

